Wave–Mean Flow Interaction Associated with a QBO-like Oscillation Simulated in a Simplified GCM

TAKESHI HORINOUCHI* AND SHIGEO YODEN

Department of Geophysics, Kyoto University, Kyoto, Japan

(Manuscript received 15 November 1996, in final form 23 June 1997)

ABSTRACT

The interaction between convectively excited waves and the mean zonal wind in the equatorial lower stratosphere is investigated with a simplified general circulation model (GCM). The model has T42 truncation, and the vertical resolution is about 700 m in the stratosphere. Although it is an "aquaplanet" model with uniform sea surface temperature, cumulus convection in low latitudes has realistic hierarchical structures with reasonable space–time spectral distributions. The model produced an oscillation having quite similar features to the equatorial quasi-biennial oscillation (QBO), although the period is 400 days.

Waves in the equatorial lower stratosphere of the model are excited mainly by the cumulus convection in low latitudes. The energy of these waves is a little larger than that observed in the real atmosphere. The dominant waves are gravity waves having an equivalent depth of about 200 m and those of 40–100 m. About half of the transport and deposition of zonal momentum contributing to the oscillation is accounted for by the gravest symmetric gravity modes: eastward momentum by Kelvin waves and westward momentum by $n = 1$ gravity waves. The momentum deposition is done over a wide range of zonal wavenumber (2–30), while about half of it is done over a period of 1–3 days. The deposition has rather continuous phase speed distributions and a considerable portion of it is provided by waves having critical levels. Since gravity waves with small intrinsic phase speeds have small vertical wavelengths, vertical grid spacings of 700 m or less appear to be required in the lower stratosphere for GCMs in order to simulate the QBO.

1. Introduction

The quasi-biennial oscillation (QBO) is an interesting phenomenon that dominates the low-frequency variability in the equatorial lower stratosphere. The first successful theory of the QBO was proposed by Lindzen and Holton (1968), who showed that the critical-level absorption of gravity waves with continuous phase-velocity distributions leads to mean flow oscillations under a suitable upper boundary condition such as the presence of the equatorial semiannual oscillation. Holton and Lindzen (1972) reformed this theory by including the dissipation of waves due to Newtonian cooling. They supposed momentum transport only by two waves: a Kelvin wave of zonal wavenumber 1 and a period of about 15 days, and a Rossby–gravity (RG) wave of zonal wavenumber 4 and a period of about 4 days. Both are dominant planetary-scale waves in the equatorial lower stratosphere and were found by Wallace and Kousky (1968) and Yanai and Maruyama (1966), respectively. The Holton–Lindzen theory was refined by Plumb (1977), who illustrated how the interaction between two internal waves and mean flow leads to an oscillation of the mean flow. This mechanism was confirmed by laboratory experiments by Plumb and McEwan (1978). Furthermore, the Holton–Lindzen theory was extended to a two-dimensional (latitude–height) model by Plumb and Bell (1982) and a three-dimensional model by Takahashi and Boville (1992). Currently, this theory is accepted as the standard theory of the QBO.

Although the QBO is undoubtedly caused by wave–mean flow interaction, observational studies have pointed out that the momentum transport by the RG waves is insufficient for driving the QBO (e.g., Lindzen and Tsay 1975). Furthermore, Dunkerton (1991) pointed out that the equatorial upwelling of the Brewer–Dobson circulation acts to reduce the downward propagation of the QBO phases. Thus, the deficit of the momentum flux became more serious. Takahashi and Boville (1992) succeeded in a three-dimensional simulation of the QBO for the first time by forcing Kelvin and RG waves near the tropopause. However, to have a QBO-like oscillation, the amplitude of the RG wave had to be about five times as large as the observational values and that of

---

* Current affiliation: Department of Atmospheric Sciences, University of Washington, Seattle, Washington.

Corresponding author address: Dr. Takeshi Horinouchi, Department of Atmospheric Sciences, University of Washington, Box 351640, Seattle, WA 98195.
E-mail: horinout@atmos.washington.edu.

the Kelvin wave also had to be (less severely) larger than the observational values, although the model did not have the Brewer–Dobson circulation.

Probable candidates for the carriers of zonal momentum in addition to these two waves are gravity waves of intermediate scales smaller than planetary scale [see Dunkerton (1997) for a review]. Recently, equatorial gravity waves have been studied intensively by radiosonde observations (e.g., Tsuda et al. 1994a,b; Maruyama 1994; Sato et al. 1994; Ogino et al. 1995). These studies have shown that gravity waves with periods less than 3 days exist ubiquitously in the equatorial lower stratosphere. Tsuda et al. (1994a,b) observed gravity waves having vertical wavelength 2–2.5 km and frequencies about 2 days by an intensive observational campaign at Watukosek, Indonesia (8°S, 113°E). Maruyama (1994) and Sato et al. (1994) analyzed long datasets of operational radiosonde observations at Singapore (1°N, 104°E). Maruyama (1994) estimated that the net eastward momentum transport by short-period (about 2 days) gravity waves is comparable to that of the long-period (7–30 days) Kelvin waves. Sato and Dunkerton (1997) estimated momentum flux of eastward- and westward-propagating waves separately and showed that the flux of short-period (1–3 days) waves is much larger than that of waves with larger periods. Thus, the momentum deposition by such short-period waves could be important for driving the QBO.

Equatorial gravity waves are also studied with aircraft and satellites. Pfister et al. (1993a,b) studied gravity waves over mesoscale cumulus systems by aircraft measurements and inferred the momentum flux associated with the observed mesoscale gravity waves. Bergman and Salby (1994) inferred the Eliassen–Palm (EP) flux propagating vertically into the stratosphere by projecting, as the proxy for cumulus heating, high-resolution global cloud imagery onto Hough functions. According to their estimation, more than half of the EP flux was accounted for by the waves with periods less than 2 days. Hayashi et al. (1984) showed that gravity waves with periods less than 2 days and zonal wavenumber 1–30 exist in the equatorial upper stratosphere and mesosphere in the GFDL "SKYHI" general circulation model (GCM).

For a long time after the proposal of the Holton–Lindzen theory, the QBO was not simulated by GCMs even though they had realistic Kelvin and RG waves (Boville and Randel 1992; Hayashi and Golder 1994) nor even though they could simulate the equatorial semiannual oscillation (Mahlman and Umshied 1984). Recently, however, Takahashi and his group succeeded in simulating the QBO by GCMs. Takahashi and Shiobara (1995) obtained a QBO-like oscillation in a numerical experiment with a spectral T106, 1/5 sector model derived from a GCM, although the oscillation was in the upper stratosphere. The model was an "aquaplanet" model with 1-km vertical grid spacing in the stratosphere without seasonal cycle. The westward acceleration in the oscillation was brought mainly by $n = 1$ gravity waves showing an anomalous spectral peak and the eastward acceleration by "random gravity waves"; the analyses were presented by Takahashi and Kumakura (1995). Takahashi (1996) succeeded in simulating the QBO by a T21 comprehensive GCM (the first version of the CCSR/NIES GCM). To produce the QBO-like oscillation he had to reduce the vertical grid spacing to about 500 m in the stratosphere and reduce the coefficients of horizontal diffusion by more than one order of magnitude. Takahashi et al. (1997) conducted further analyses of this oscillation and inferred that the westward acceleration was due to westward-propagating $n = 1$ gravity waves, westward-propagating "random gravity waves," and Rossby waves, while the eastward acceleration was due to Kelvin waves and eastward-propagating gravity waves, although they were not shown very clearly.

It seems natural that Takahashi (1996) had to increase the vertical resolution in order to produce the oscillation, since, in general, the vertical resolutions of GCMs are too coarse to resolve the waves in the equatorial stratosphere. The vertical resolutions are usually determined on the basis of mid- and high latitudes. For example, the SKYHI GCM has the vertical grid spacing about 2 km in the stratosphere. As shown by Boville and Randel (1992), this resolution is insufficient to simulate the divergence of the momentum flux of equatorial waves. On the other hand, it is less certain why he had to reduce the horizontal diffusion coefficients in order to get the oscillation.

The studies mentioned in this section lead to the following problems to be considered:

- What waves drive the QBO in the real atmosphere?
- What is required for GCMs to produce the QBO?

In this study, we obtained a quite realistic QBO-like oscillation in a simplified GCM. Thus, the wave–mean flow interaction driving the oscillation is studied in detail. The horizontal resolution of the model is T42, and the vertical resolution is about 700 m in the stratosphere, which is as small as that used by Takahashi (1996). On the other hand, the horizontal diffusion coefficients are not reduced. We investigated which kind and what amount of waves exist in the equatorial lower stratosphere of the model and how these waves drive the oscillation. Then, we examined the problems above.

The model is described in section 2. Climatology and moist convection in the model are presented in section 3. In section 4, waves in the equatorial lower stratosphere are analyzed in physical space and wavenumber-frequency space. Analyses of the EP flux and its relation to the QBO-like oscillation are presented in section 5. In these two sections, some comparisons with observational studies are also made. The results are discussed in section 6, where necessary conditions to simulate the QBO in a GCM are discussed, as well as the implications for waves driving the QBO in the real atmosphere. Conclusions are given in section 7. Appendices describe analysis methods.

2. Model description

The model used in this study is derived from an atmospheric GCM (AGCM5) in the GFD-DENNOU Library. It is a spectral model with a triangular truncation of T42 (the maximum "total wavenumber" is equal to 42). For the vertical coordinate, $\sigma \equiv p/p_s$ is used (p_s is surface pressure). The model has 40 vertical levels; the vertical grid spacing is about 0.4 km near the surface, about 1.5 km in the middle troposphere, and about 0.7 km in the stratosphere (see tick marks inside the vertical axes in Fig. 4). Since the static stability in the stratosphere is larger than that in the troposphere, it is natural to take higher vertical resolution in the stratosphere. The highest four levels of $\sigma < 0.01$ ($p < 10$ hPa) are sponge layers, where the Rayleigh friction with *e*-folding time 0.4 days is incorporated. Time integration is done with the semi-implicit scheme with time increment 15 min.

The moist convective adjustment (MCA) scheme with a critical relative humidity of 0.99 is used as cumulus parameterization. In addition, the large-scale condensation scheme (condensation at each grid point) and the dry convective adjustment scheme are applied after the MCA for each time step. Horizontal diffusion proportional to ∇^6 is used; the *e*-folding time for the maximum total wavenumber is 12 h. The coefficient of vertical diffusion is set equal to 0.1 $m^2\ s^{-1}$. For the surface processes, the bulk method with the coefficients for the neutral stratification with roughness length 0.1 mm is used. The whole globe is assumed to be covered with the ocean (aquaplanet) with uniform sea surface temperature (SST) of 300 K, so that no baroclinic instability occurs in this model. Radiative processes in the troposphere are replaced with a simple globally uniform cooling rate; the atmosphere below $\sigma = 0.25$ ($\approx$250 hPa) is cooled by 0.8 K day^{-1}, and the cooling rate is reduced linearly with $-\ln\sigma$ from $\sigma = 0.25$ to $\sigma = 0.19$, and no uniform cooling is incorporated above this level. Radiative processes in the stratosphere are replaced with Newtonian cooling; the *e*-folding time is 40 days for $\sigma = 0.15$–0.13 and is 20 days above that. The basic temperature for Newtonian cooling is 198 K below $\sigma = 0.11$ and increase linearly with $-\ln\sigma$ so that it is 250 *K* at $\sigma = 0.005$. Because of the constant SST and the horizontally uniform radiative processes, this model has no external horizontal asymmetry except for the earth's rotation.

Originally, these horizontally symmetric thermal conditions are chosen to suppress the baroclinic waves in midlatitudes. The model was arranged to analyze the stratospheric waves excited by tropical cumulus convection. Thus, we wanted to suppress the possible secondary waves that are excited by baroclinic waves and propagate into the equatorial stratosphere. Although our choice is rather strange for a GCM, the model reproduced realistic features of the tropical cumulus convection as shown in section 3. Thus, we retained the original choice in this study. Note that the most important tropospheric process for the QBO is the tropical cumulus convection, which excites the waves driving the QBO.

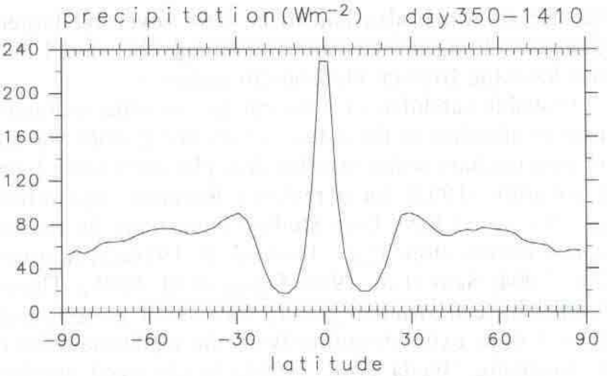

FIG. 1. Time-averaged zonal-mean precipitation (W m^{-2}) from day 350 to day 1410.

The initial state is an isothermal atmosphere at rest. For the first 100 days, time integration was done with the T10 version of the model (the same model except for the horizontal resolution being T10). Then the model was replaced with the T21 version; the output of the T10 model was interpolated and passed to the T21 version and the integration was done until day 275. Finally, the T21 model was replaced with the T42 version and an adjustment integration was done for 75 days. Thus, the data from day 350 are used for the analyses; the length of the data set is 1060 days (up to day 1410). The outputs were sampled every 3 h for the periods intensively analyzed in the following.

3. Climatology in the equatorial region

a. Cumulus convection

The waves propagating into the equatorial stratosphere of this model are excited by cumulus convection represented by the MCA. Although there is no external asymmetry except for the earth's rotation, the cumulus convection in low latitudes has different form from that in mid- and high latitudes due only to this asymmetry. In mid- and high latitudes (poleward of about 20°) most of moist convection has structures similar to tropical cyclones; the vorticity in the lower levels has high correlation to the precipitation, which is organized circularly with a diameter of about 1000 km and a duration of over a week. On the other hand, precipitation in low latitudes is not so persistent and has realistic features as the cumulus convective systems over the tropical ocean, as shown in the following of this section.

Figure 1 shows the time-averaged zonal-mean precipitation. The precipitation is largest on the equator and smallest between 10° and 20° since the Hadley circulation exists between $\varphi = \pm 20°$ despite the uniform

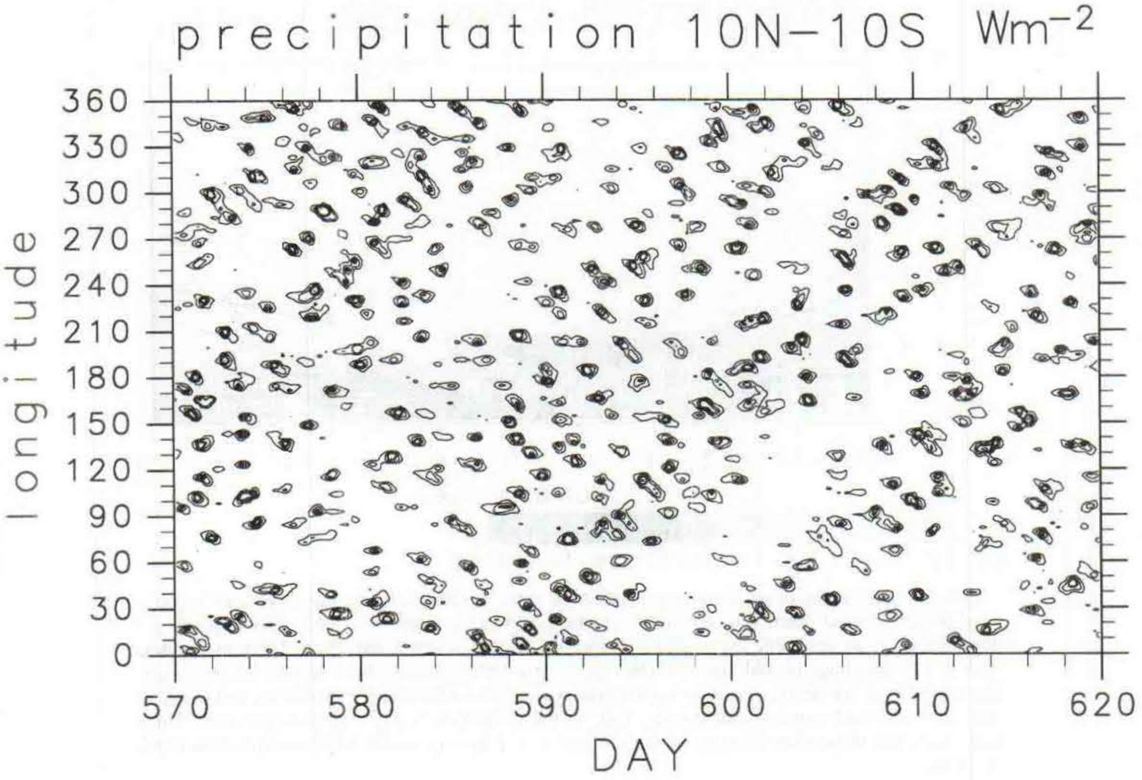

FIG. 2. Time–longitude section of precipitation averaged over $|\varphi| \leq 10°$ (W m^{-2}). Contours are log-scaled [$(1, 2, 5) \times 10^n$] with the minimum value 200 W m^{-2}.

SST. The maximum precipitation intensity of 2.3×10^2 W m^{-2} (2.9 m/year) at the equator is within the climatological values in the intertropical convergence zone (ITCZ; see, e.g., Peixoto and Oort 1992, their Fig. 7.24). The averaged precipitation intensity of 1.0×10^2 W m^{-2} for $|\varphi| \leq 10°$ is slightly smaller than the climatological value. It is also smaller if averaged over $|\varphi| \leq 15°$.

Figure 2 shows a time–longitude section of precipitation averaged over $|\varphi| \leq 10°$. Small-scale westward-moving structures exist in large-scale eastward-moving structures. This is similar to the cumulus convective systems commonly observed over the tropical ocean (Nakazawa 1988): westward-moving cloud clusters exist in eastward-moving structures from super cloud clusters to planetary-scale intraseasonal oscillations. In this model, the westward-moving "cloud clusters" have larger scales than those in the real atmosphere, which is a natural consequence of the low resolution of T42. On the other hand, their duration has some realistic values of 1–2 days.

Figure 3 shows the power spectral density of vertically averaged cumulus heating (condensation heating due to the MCA) in low latitudes. This figure shows an ensemble average of five analyzed periods. However, the following features are observed in each period too. The overall feature of the spectrum is white with respect to zonal wavenumber and red with respect to frequency. In addition, there are spectral peaks that indicate an organization along the dispersion curves of equatorial gravity waves with an equivalent depth h about 20 m.

Such a spectral organization exists in the real atmosphere. Takayabu (1994a,b) showed that cumulus convective systems over the tropical Pacific are organized along the dispersion curves of equatorial waves (Kelvin, RG, inertia–gravity, and Rossby waves of small n's) with $h \approx 20$ m. The same feature is clearly seen in Fig. 3 for Kelvin and $n = 1$ gravity waves. There also are small spectral peaks at zonal wavenumbers 0 and +1 coinciding with the dispersion relations of the RG wave with $h = 20$ m although the dispersion curve for the RG wave is not shown in Fig. 3. All of these spectral peaks are found in the spectra of horizontal wind in the troposphere (not shown). The spectral peak along the dispersion curve of the Kelvin wave corresponds to the tropical intraseasonal oscillation (Madden and Julian 1972), whose phase speed of 15 m s^{-1} is similar to observational values. Note, for reference, that the equatorial radius of deformation l_e for $h = 20$ m is 0.78×10^6 m, where $l_e \equiv (gh)^{1/4}\beta^{-1/2}$ (g is gravity, β is the meridional gradient of the Coriolis parameter).

b. Zonal-mean state in the equatorial region

Figure 4a shows time-averaged zonal-mean temperature. The tropopause is coldest near the equator because

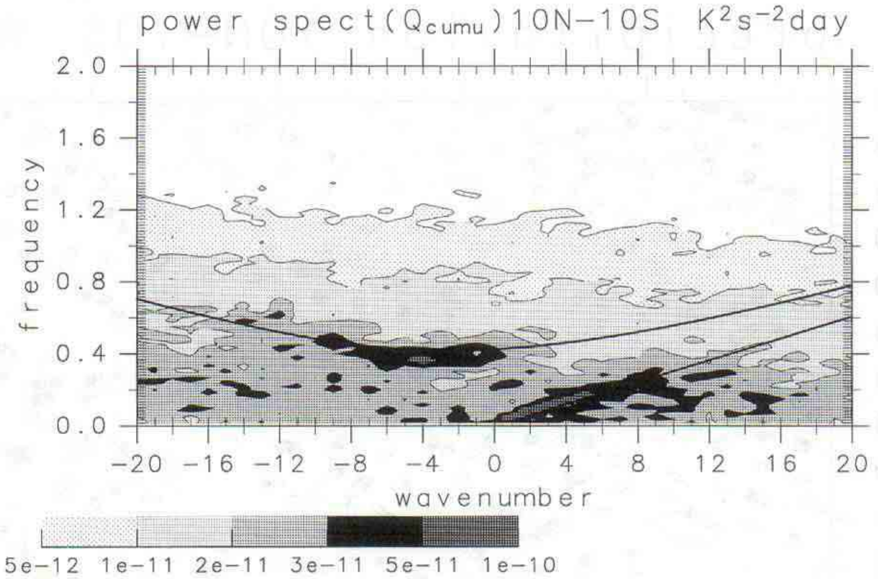

FIG. 3. Zonal wavenumber-frequency distribution of the meridionally averaged ($|\varphi| \leq 10°$) space–time power spectral density of the mass-weighted vertical average of cumulus heating (K^2 s^{-2} day). Shown is an ensemble average of five spectra, each of which is calculated from 60-day data with a 3-h sampling. In addition, the three-point smoothing is done with respect to frequency. See appendix A for details. Positive wavenumbers are eastward-moving components and negative ones are westward-moving components. Unit of the frequency is day^{-1} (cycles per day). Thick lines show the dispersion relations of Kelvin and $n = 1$ gravity waves with an equivalent depth of 20 m.

of the Hadley circulation. Figure 4b shows two buoyancy frequencies averaged over $|\varphi| \leq 10°$: the log-pressure buoyancy frequency (see Andrews et al. 1987) for the log-pressure scale height $H = 7000$ m and the ordinary local buoyancy frequency. These two frequencies are different by the ratio of the local scale height to H. The buoyancy frequencies are comparable to those in the real atmosphere, although they are a little smaller in the upper troposphere.

This model produced a QBO-like oscillation in the equatorial lower stratosphere. Figure 5 shows the time–height section of zonal-mean zonal wind over the equator. The highest two grids of the model are not shown and the highest two grids in the figure are in the sponge layer where the mean zonal wind is very weak due to the Rayleigh friction. A QBO-like oscillation (hereafter, sometimes referred to simply as QBO) with a period of about 400 days is clearly seen in the lower stratosphere. Although the period is about half of the QBO in the real atmosphere, it might be doubled if a realistic Brewer–Dobson circulation is incorporated (see section 6a). The maximum speed of the easterly wind (28 m s^{-1}) is larger than that of the westerly wind (22 m s^{-1}), both of which are close to the observed values (35 m s^{-1} and 20 m s^{-1}, respectively; see Naujokat 1986). The peak eastward mean flow accelerations are larger than the peak westward accelerations, and the downward propagation of the westerly shear zones (westerly in the upper levels and easterly in the lower levels) is faster than that of the easterly shear zones.

Figure 6 shows zonal-mean zonal wind averaged over days 570–630 and 750–810 (periods I and II, respectively; see Fig. 5). Period I is in a westerly shear phase of the QBO, while period II is in an easterly shear phase. The meridional width of the QBO is similar to that in the real atmosphere. The eastward acceleration when the westerly wind appears is concentrated near the equator, while the westward acceleration at the opposite QBO phase is rather broad (not shown), as is observed (Hamilton 1984; Dunkerton and Delisi 1985).

All of these results show that the QBO-like oscillation in this model is quite realistic. Among the simulated QBO-like oscillations with GCMs, this is the first one that reproduced the observed asymmetry of the easterly and westerly wind maxima; in both of the QBO-like oscillations obtained by Takahashi and Shiobara (1995) and Takahashi (1996), easterly winds are weaker than westerly winds. This asymmetry is discussed further in section 6g.

As shown in Figs. 5 and 6, zonal-mean zonal wind in the equatorial upper troposphere is westerly unlike the real atmosphere. Time-averaged zonal wind around $\sigma = 0.07$ (70 hPa) over the equator is also westerly. There is no realistic jet stream in midlatitudes in this model because of the uniform SST. The mean zonal wind in midlatitudes is weak easterly, being maximum at about $\varphi = \pm 30°$ and $\sigma \approx 0.1$. On the other hand, it is westerly around $\varphi = \pm 15°$ in the troposphere because of the Hadley circulation.

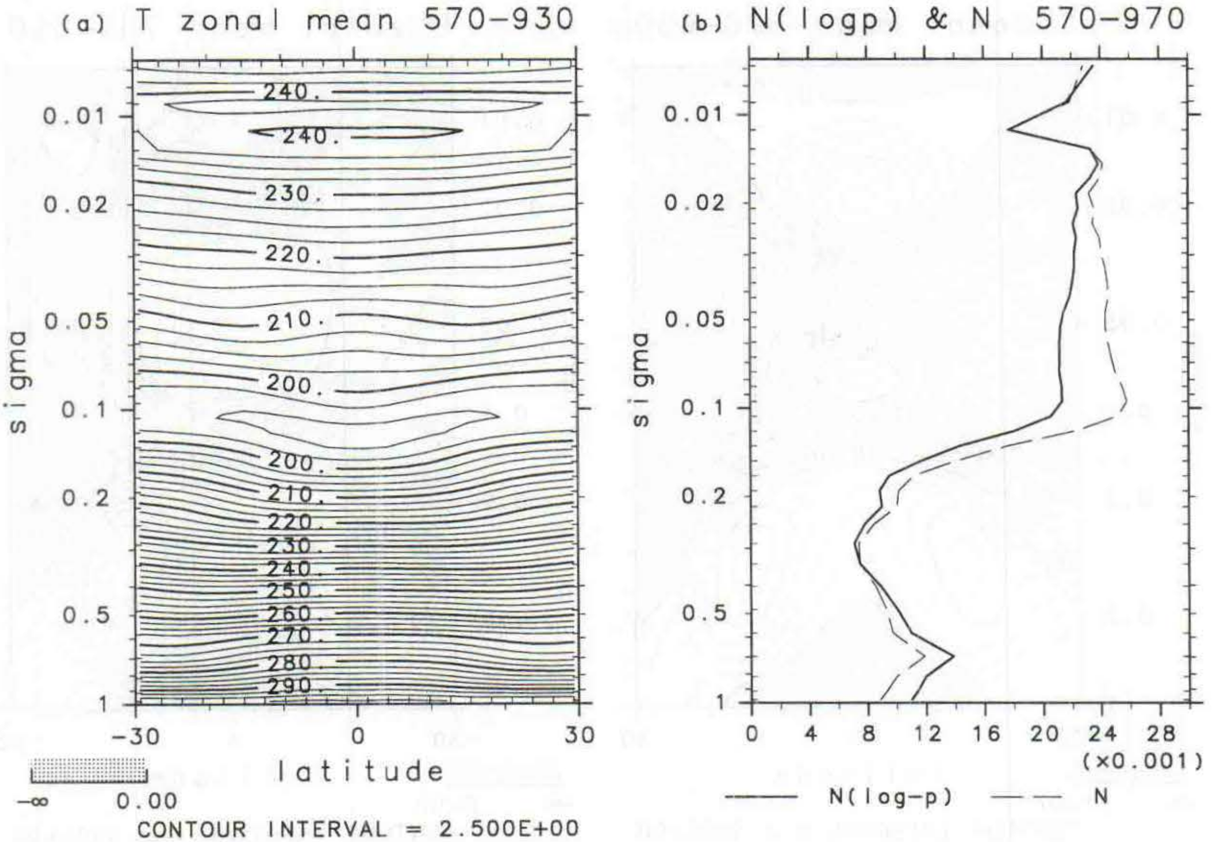

FIG. 4. (a) Latitude–height section of zonal-mean temperature (K) averaged over days 570–930. (b) Height section of the log-pressure buoyancy frequency (solid line) and the ordinary local buoyancy frequency (dashed line) (s^{-1}) averaged over $|\varphi| \leq 10°$ for the same period. The log-pressure scale height is set equal to 7000 m. The ordinate is σ. Tick marks inside the vertical axes indicate the vertical levels of the model and the highest two grids above $\sigma = 0.005$ are out of the range.

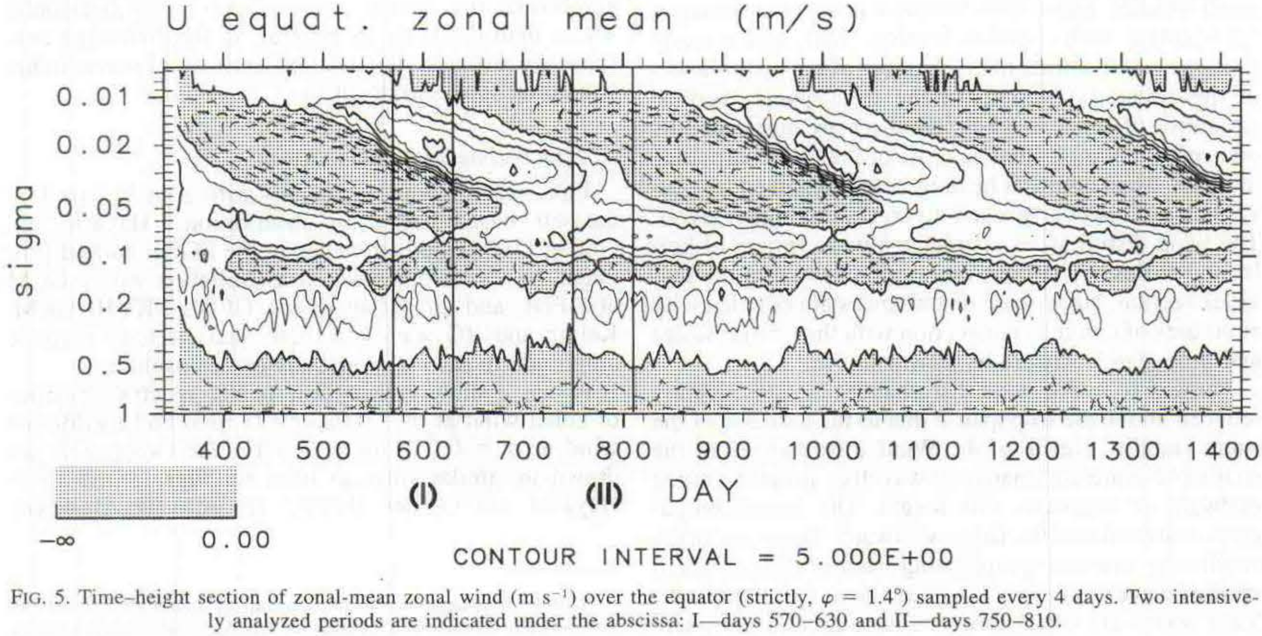

FIG. 5. Time–height section of zonal-mean zonal wind (m s^{-1}) over the equator (strictly, $\varphi = 1.4°$) sampled every 4 days. Two intensively analyzed periods are indicated under the abscissa: I—days 570–630 and II—days 750–810.

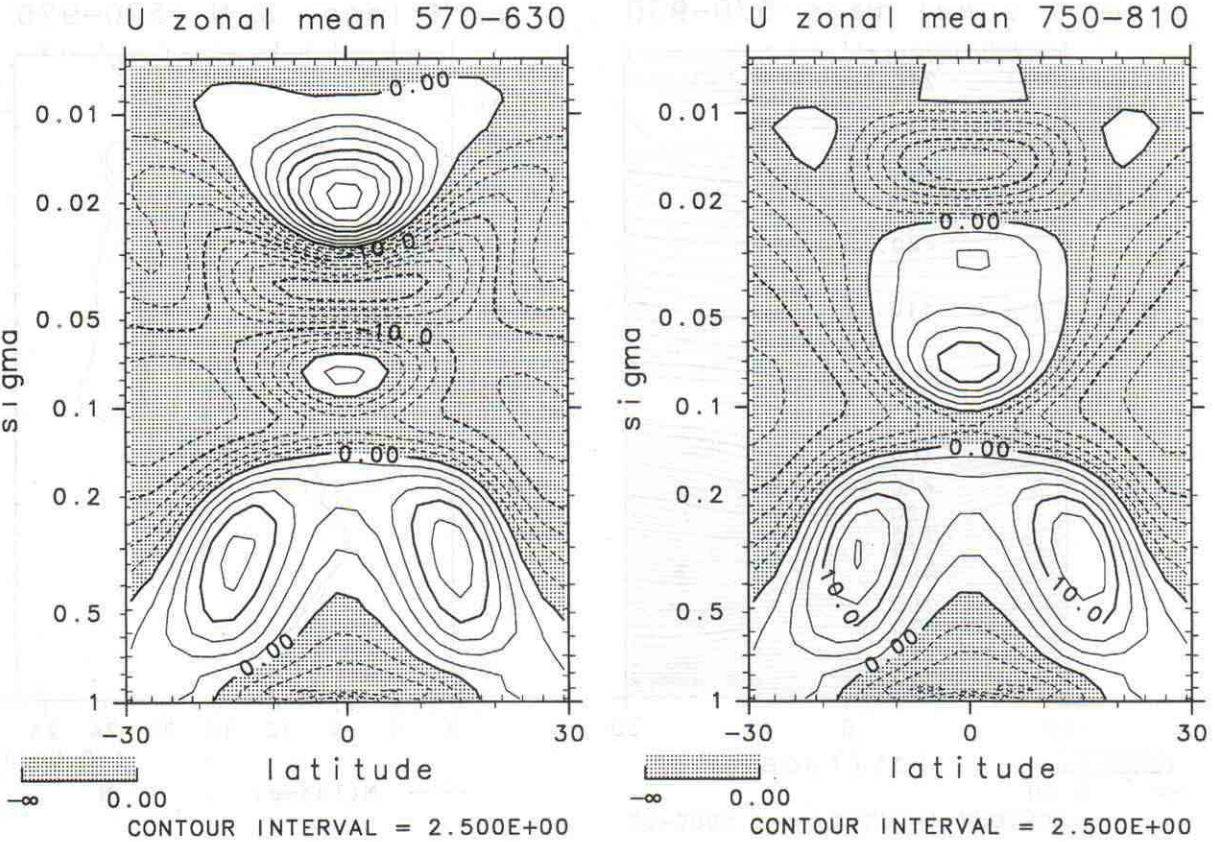

FIG. 6. Latitude–height section of time-averaged zonal-mean zonal wind (m s^{-1}) for period I (left) and period II (right).

4. Wave analyses

a. An overview

Figure 7 shows an example of vertical sections of zonal wind deviation from the zonal mean over the equator, together with cumulus heating. With such a snapshot, we can illustrate many features of the disturbances in the equatorial region. In the troposphere, vertical structures of zonal wind disturbances are dominated by one-cell structures—that is, those of the "first baroclinic modes." Most cumulus heating is accompanied by convergence in lower levels and divergence in higher levels. The wind disturbances also have a wide variety of horizontal scales as cumulus convection shown in the previous section; large-scale disturbances are coupled with structures of cumulus convection with the similar scales and propagate eastward as shown in Fig. 2.

Vertical scales of wind disturbances are significantly reduced above the tropopause due to the increase of the static stability (see Fig. 4). Wind disturbances in the stratosphere are dominated by wavelike structures tilted eastward or westward with height. The former propagates eastward and the latter westward. There are large-amplitude eastward-propagating waves having small vertical wavelength (≈5 km) just above the tropopause. Such waves are often observed in the real atmosphere too (Nishi and Sumi 1995). In this model these waves seem to be closely related to the tropospheric "intraseasonal oscillation" (section 3a). Above these levels, eastward- and westward-propagating waves have similar amplitude; the former waves have larger horizontal scales than the latter in general. In the following sections, we will describe detailed analyses of waves in the equatorial lower stratosphere.

b. Space–time spectral analyses

First, we compare our results with a study based on datasets based partly on observations; Hayashi and Golder (1994) studied waves in the FGGE dataset produced by a four-dimensional assimilation with a GCM at GFDL and an output of the GFDL SKYHI GCM. Kelvin and RG waves in these datasets have realistic amplitude in the equatorial lower stratosphere.

Figure 8 shows space–time power spectral densities of zonal wind at $\sigma = 0.023$ (≈23 hPa) and meridional wind at $\sigma = 0.047$ for period II. The two panels are drawn in similar ways as used for Figs. 3 and 15 in Hayashi and Golder (1994),[1] respectively. However,

---

[1] Due to a typographical error, the unit in their Fig. 3 is 1/10 of that shown in the caption (Y. Hayashi 1996, personal communication).

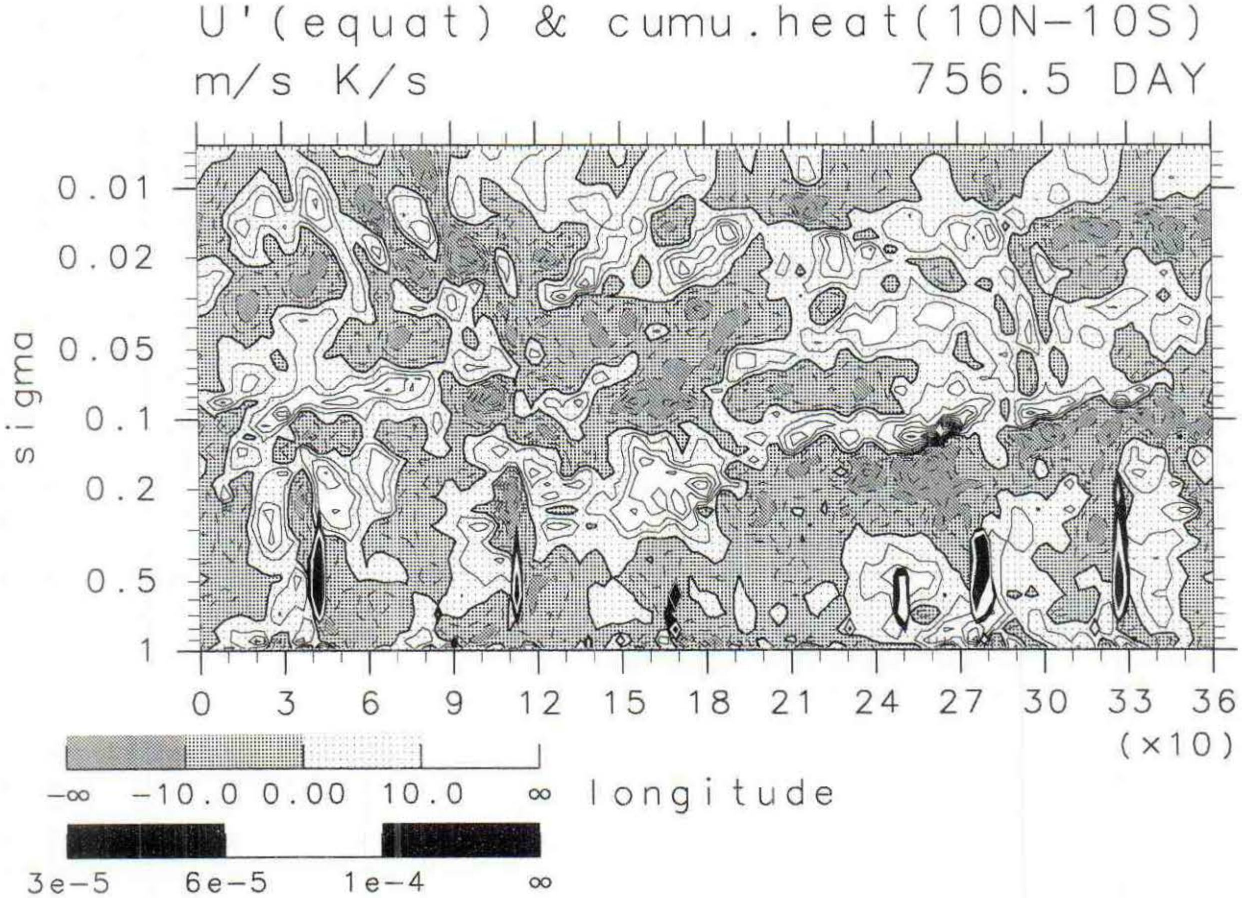

FIG. 7. Longitude–height section of zonal wind deviation (m s^{-1}) from the zonal mean over the equator (gray scaling with contours: contour interval is 5 m s^{-1}) and cumulus heating (K s^{-1}) averaged over $|\varphi| \leq 10°$ (black and white tones) at day 756.5.

since they showed spectra for zonal wavenumbers less than 10 and frequencies less than 0.5 day^{-1} (cycles per day), the comparison is possible only within this range. The phase of the QBO-like oscillation in period II is similar to that of the QBO in the FGGE observational period (December 1978–November 1979). In addition, zonal-mean wind in the equatorial lower stratosphere in period II is relatively small. Thus, in this section, we present the results with data of this period.

The spectra obtained in our model have larger mag-

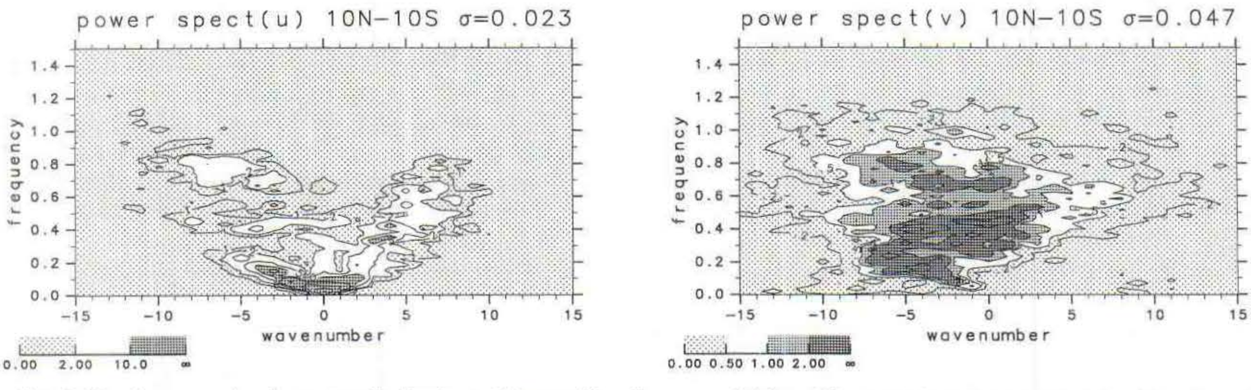

FIG. 8. Zonal wavenumber-frequency distributions of the meridionally averaged ($|\varphi| \leq 10°$) space–time power spectral densities of zonal wind at $\sigma = 0.023$ (left) and meridional wind at $\sigma = 0.047$ (right) for period II (m^2 s^{-2} day). The three-point smoothing (appendix A) is done with respect to frequency. The minimum values of the log-scaled contours $[(1, 2, 5) \times 10^n]$ are 1 (left) and 0.2 (right). Note that the shadings, which differ with the two panels, are corresponding to Figs. 3 and 15 in Hayashi and Golder (1994).

nitude than those for the FGGE and SKYHI datasets. As for eastward-moving components of zonal wind spectrum, the power is 1–3 times larger than that for the SKYHI dataset (it is larger especially for large wavenumbers, while they are similar for $s = 1$), which, in turn, is larger than that of the FGGE dataset. As for westward-moving components, on the other hand, the power is 1–2 times larger than that for the FGGE dataset, which, in turn, is larger than that for the SKYHI dataset. The spectra of meridional wind in the model have also larger magnitude than that of the SKYHI and FGGE datasets. These results suggest that kinetic energy of waves in our model may be somewhat larger than in the real atmosphere. Note, however, that the vertical resolutions of the two GFDL models are too coarse to reproduce the entire spectra in the equatorial lower stratosphere. Thus, studies with these models might underestimate the power of the waves in this region.

To examine wavenumber and/or frequency distributions of wave amplitude or wave energy, it is convenient to use the energy content form for spectral presentation (appendix A). Figure 9 shows space–time power spectral densities in this form. Since the QBO-like oscillation below $\sigma = 0.095$ (about 17 km) is very weak, the spectra at this level (upper panels) are nearly independent of the QBO phase. For small zonal wavenumbers less than 5, the power of the eastward-moving disturbance is dominant in two regions: one having roughly constant phase velocities of about 20 m s^{-1} and the other having roughly constant frequencies of $f \approx 0.5$ day^{-1}. The former is due to Kelvin waves and the latter is due to inertia–gravity waves, as is shown in section 4c. These two regions join at higher wavenumbers. The power of the westward-moving components show similar features. However, westward-moving disturbances with $s < 10$ and $f < 0.3$ day^{-1} are identified mainly as Rossby waves, while those with $f > 0.3$ day^{-1} are identified mainly as inertia–gravity waves (sections 4c and 4d). Frequency spectrum of eastward-moving components is large between 0.3 and 0.6 day^{-1}, while that of westward-moving components is large between 0.4 and 0.8 day^{-1}. Zonal wavenumber spectra show wide distributions of both eastward- and westward-moving components over $s = 1$–20. For the eastward-moving components, spectral distribution is rather uniform over $s = 1$–15 and decreases in larger wavenumbers. Whereas, that of westward-moving components shows a maximum at $s = 6$.

The overall features of the spectrum at $\sigma = 0.023$ (about 26 km) shown in the lower panels in Fig. 9 are similar to those at $\sigma = 0.095$ described above, although there are some quantitative differences. Eastward-moving components with phase speeds of about 20 m s^{-1} are smaller than those at $\sigma = 0.095$, while westward-moving components are larger. Such quantitative differences are dependent on the QBO phase; in period II, westerly wind in the lower part of the lower stratosphere selectively damps eastward-propagating waves. Vertical propagation of equatorial waves depending on the QBO phases is described in section 5.

The frequency spectra at $\sigma = 0.023$ are compared with the observed spectra presented by Sato and Dunkerton (1997, hereafter SD97) and Sato et al. (1994); they showed frequency spectra averaged over 20–25 km, which were derived from long-term twice-daily radiosonde data at Singapore. The frequency spectra of the model have large power at $0.3 < f < 1$ day^{-1}, where the maximum value is more than 20 m^2 s^{-2} for both eastward- and westward-propagating waves. The spectral power seems to be about three times larger than the observed value for these high frequencies, while it is comparable to the observation for $f \approx 0.1$ day^{-1}.

c. Energy of Hough modes

In order to investigate the meridional structures of the disturbances in the equatorial lower stratosphere, wave energy of each meridional mode is estimated using the expansion by Hough functions as described in appendix B. Strictly speaking, this expansion is meaningful only for conservative linear waves in a resting or rigidly rotating basic wind. However, it is verified that this expansion is effective for gravity modes with small n's if an appropriate speed is chosen for the rigidly rotating basic wind. Here the results for the data of period II are presented as in the previous section. The velocity of the rigidly rotating basic wind used here is -3, 3, 3, 3, and 0 m s^{-1} at the equator for 95, 67, 47, 33, and 23 hPa, respectively; these values are determined subjectively but the results are not very sensitive to the difference of these values of about 5 m s^{-1}.

Figure 10 shows zonal wavenumber-frequency distributions of meridionally averaged total wave energy $\langle E \rangle$ [see Eq. (B2)] of gravity modes of small n's: Kelvin ($n = -1$), RG ($n = 0$), and inertia–gravity waves of $n = 1$–4 at 23 hPa. Here, for convenience, RG waves are classified as gravity modes even when they propagate westward. Obviously, the dominant eastward-propagating mode is the Kelvin wave and the dominant west-

→

FIG. 9. Zonal wavenumber–frequency distributions of the meridionally averaged ($|\varphi| \leq 10°$) space–time power spectral densities of horizontal velocities: summation of the spectra of zonal and meridional winds for period II (m^2 s^{-2}). The upper half shows spectra at $\sigma = 0.095$ ($\approx$95 hPa) and the lower half shows those at $\sigma = 0.023$ ($\approx$23 hPa). The left half shows westward-moving components and the right half shows eastward-moving components. Color panels are space–time spectra, where thin solid lines indicate constant zonal phase speeds of 20 and 40 m s^{-1}. Colors are scaled logarithmically. Bottom panels are zonal wavenumber spectra obtained by integrating the space–time spectra with frequency. Left and right panels are frequency spectra obtained by integrating the space–time spectra with zonal wavenumber. All of these are shown in the energy content form.

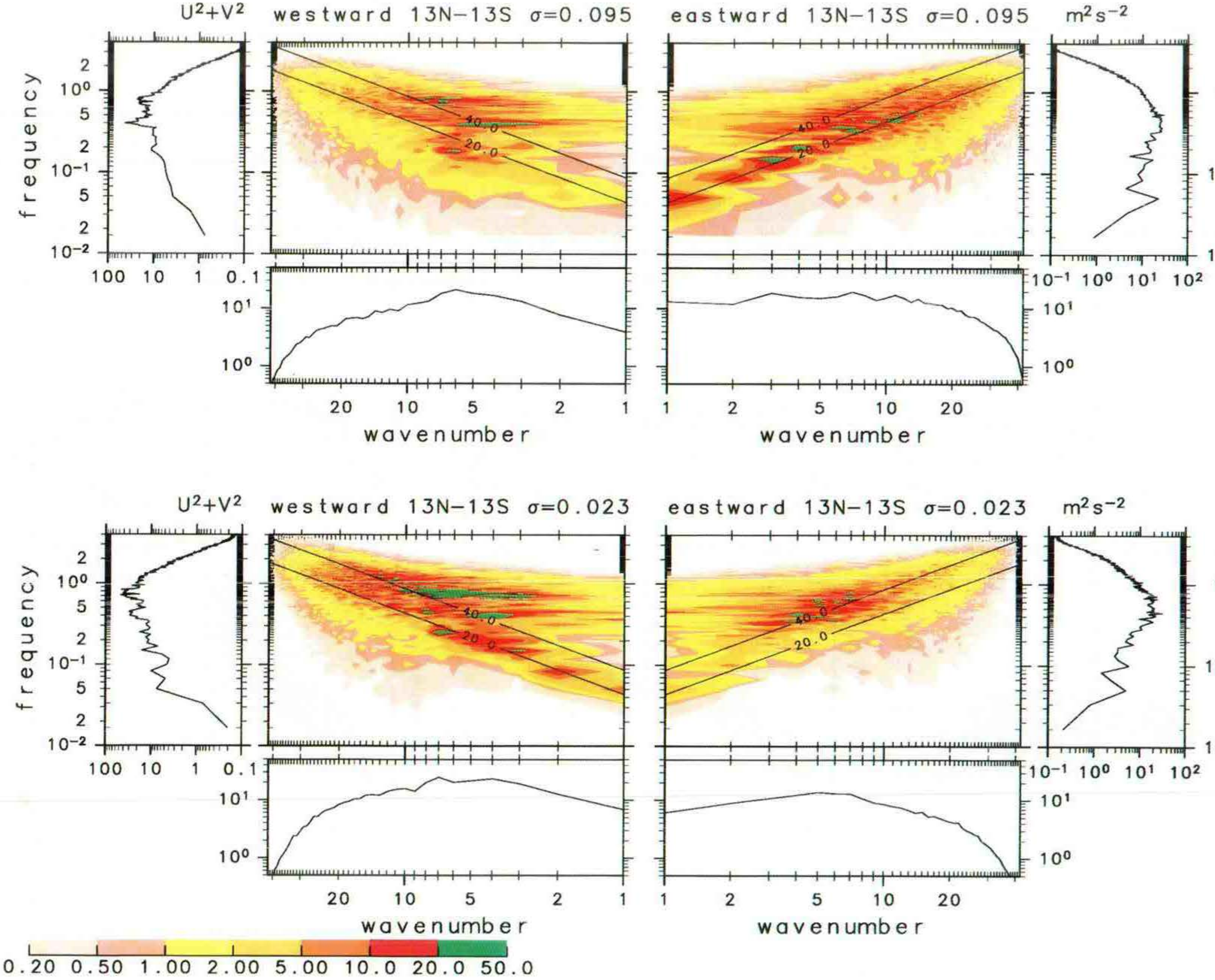
U²+V²
westward 13N–13S σ=0.095
eastward 13N–13S σ=0.095
m²s⁻²
frequency
wavenumber
40.0
20.0
westward 13N–13S σ=0.023
eastward 13N–13S σ=0.023
0.20 0.50 1.00 2.00 5.00 10.0 20.0 50.0

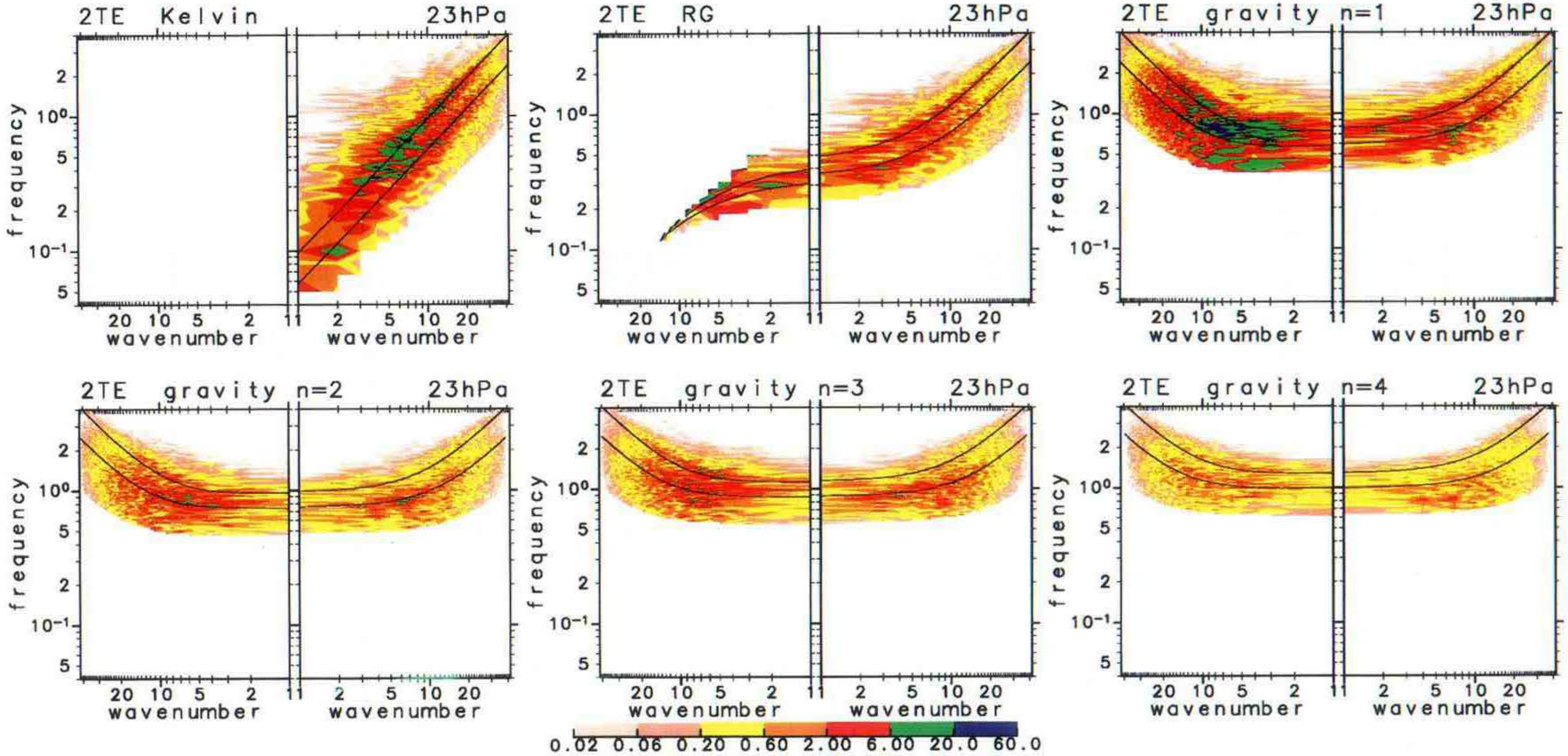

FIG. 10. Zonal wavenumber–frequency distributions of the meridionally averaged total energy projected onto Hough modes ($\langle E \rangle$) at 23 hPa for period II. Those for Kelvin wave, RG wave, and inertia–gravity waves of $n = 1$–4 are shown. Thin solid lines show the dispersion relation of each mode with the equivalent depth of 70 m (lines with lower frequencies) and 200 m (higher frequencies).

ward-propagating mode is the $n = 1$ gravity wave. Thin solid lines in each panel show the dispersion curves of each mode with equivalent depths h 70 and 200 m. The spectrum of each mode has two dominant regions roughly along these lines. That is, there are two characteristic equivalent depths at this height. The corresponding figure for 95 hPa (not shown) also indicates the dominance of two equivalent depths. However, the dominant equivalent depths are about 50 and 200 m; the larger one is unchanged throughout the lower stratosphere ($h \approx 200$ m) while the smaller one increases with height from 40 to 100 m. Such a splitting due to two dominant equivalent depths is faintly observed in Figs. 9 and 17. Note, for reference, that $l_e = 0.98$, 1.1 and 1.4×10^6 m for $h = 50$, 70, and 200 m, respectively; thus, the modes with these equivalent depths and small n's are trapped within low latitudes.

The dominance of two equivalent depths can be interpreted in terms of the characters of atmospheric responses to transient heating in the troposphere. The waves that effectively respond to the heating are those having vertical wavelengths in the troposphere about twice the vertical scale of the heating. The dominance of $h = 200$ m is interpreted by this fact [Hayashi (1976), Salby and Garcia (1987), and see Horinouchi and Yoden (1996) for a thorough explanation]. On the other hand, the equivalent depths of $h = 40$–100 m may be dominant because the frequency spectrum of the thermal forcing in the troposphere is red; that is, although these waves do not respond effectively, their amplitude can be large when the forcing is large. Since waves with smaller equivalent depths have smaller vertical group velocities, they are damped in lower altitudes so that the smaller dominant equivalent depths increase with height.

Figure 11 shows the total wave energy of each gravity mode integrated over zonal wavenumbers and frequencies. Symmetric modes with respect to the equator (n: odd numbers) have larger energy than antisymmetric modes. Kelvin and $n = 1$ gravity waves are dominant, and the wave energy decreases with n. The Kelvin waves account for 60% of the energy of eastward-propagating gravity waves at 95 hPa in the lowest part of the stratosphere, while $n = 1$ gravity waves account for 50% of the energy of westward-propagating gravity waves at 95 hPa. These percentages are somewhat smaller in higher altitudes.

d. Vertical structures

Vertical structures of various waves can be elucidated with appropriate space–time filters. Figure 12 shows time–height sections of some filtered zonal wind disturbances at a given longitude $\lambda = 0°$ over the equator. As expected from the spectral analyses, the first four panels consist mainly of gravity waves, while the last panel consists mainly of Rossby waves; this is confirmed by comparing the vertical wavelengths estimated from the figure with theoretical vertical wavelengths estimated from the dispersion relation.

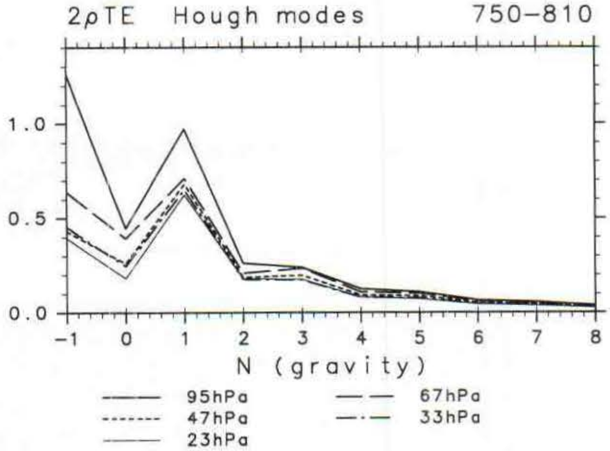

FIG. 11. Mass-weighted (multiplied by $p/1000$) $\langle E \rangle$ ($\mathrm{m^2\ s^{-2}}$) of Hough modes integrated over the whole frequencies and zonal wavenumbers at 95, 67, 47, 33, and 23 hPa for period II. The abscissa is the meridional mode number n, where odd modes are symmetric and even modes are antisymmetric with respect to the equator. Only the gravity modes of small n's are shown [Kelvin wave ($n = -1$), RG wave ($n = 0$), inertia–gravity waves of $n = 1$–8].

In general, eastward-propagating gravity waves (Figs. 12a,b) have larger periods than westward-propagating ones (12c,d), as expected from Fig. 9. The vertical wavelength of slow eastward-propagating waves (12a) are about 5–7 km in the stratosphere. The amplitude of these waves is large just above the tropopause and decreases rapidly with height. On the other hand, typical vertical wavelength in (12b) is more than 10 km, and the amplitude does not decrease with height. The vertical wavelengths of westward-propagating gravity waves are similar to the eastward-propagating ones: 5–6 km for slow waves (12c) and about 10 km for fast waves (12d). This dependence of vertical wavelength on phase velocity is explained by the linear theory of gravity waves: gravity waves of small phase speeds (12a,c) are expected to have small equivalent depths, thus having small vertical wavelengths. In addition, they have small vertical group velocities and are susceptible to critical level absorption.

Low-frequency disturbances in the stratosphere shown in Fig. 12e mainly consist of Rossby waves. The vertical wavelengths are too large for gravity waves of phase speeds about 20 m $\mathrm{s^{-1}}$ (see Fig. 9). The source of these Rossby waves is mainly in midlatitude troposphere as described in section 5. Thus, these waves are not realistic because the midlatitude processes of this model are not realistic.

5. Eliassen–Palm flux and its relation to the QBO-like oscillation

The relation between various waves and the QBO-like oscillation is investigated by computing Eliassen–

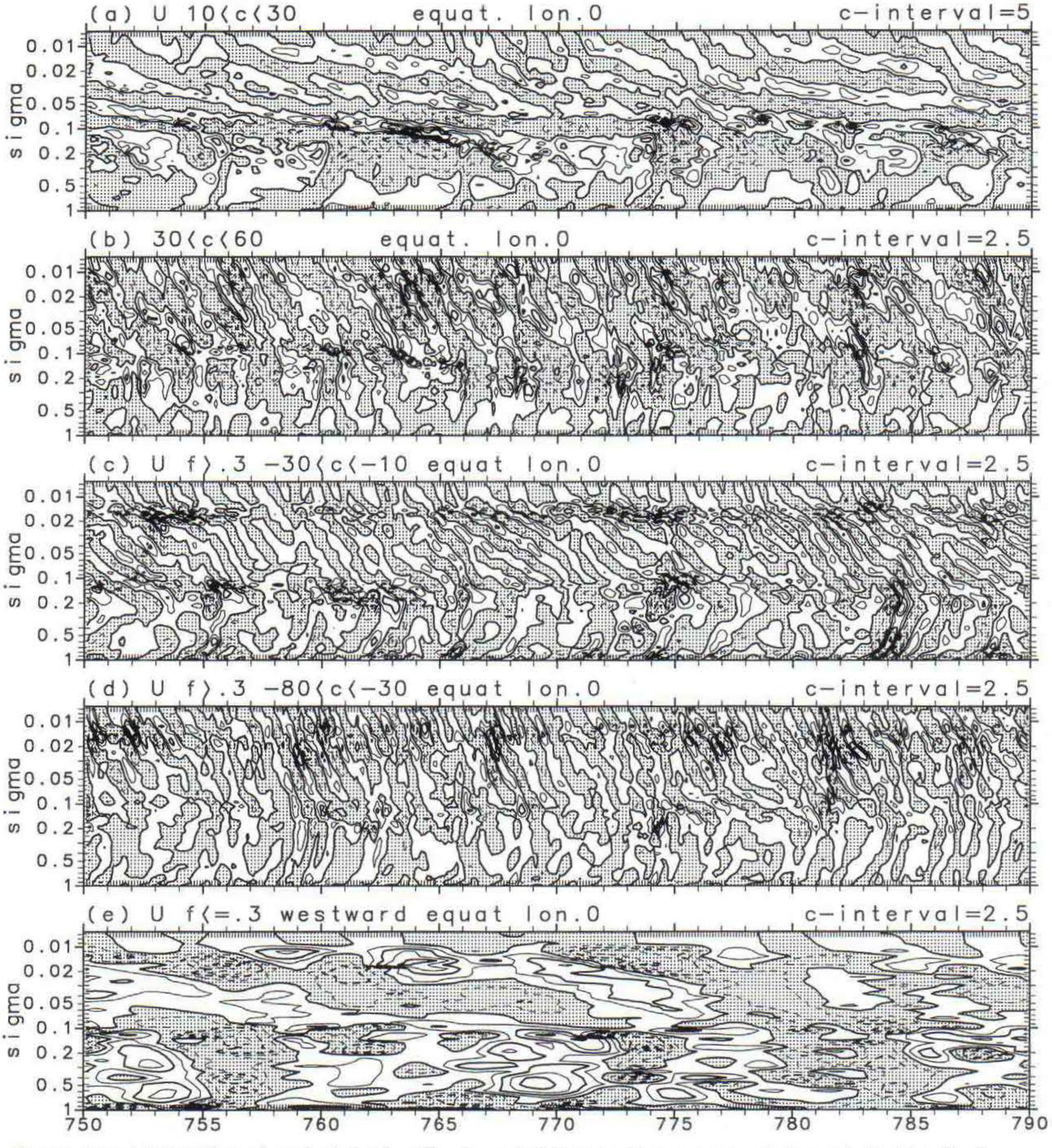

FIG. 12. Time–height sections of zonal wind at $\lambda = 0°$ and $\varphi = 1.4°$ filtered with respect to zonal phase velocity (c) and/or frequency (f): (a) $10 < c < 30$ m s^{-1}, (b) $30 < c < 60$ m s^{-1}, (c) $-30 < c < -10$ m s^{-1} and $f > 0.3$ day^{-1}, (d) $-80 < c < -30$ m s^{-1} and $f > 0.3$ day^{-1}, and (e) $c < 0$ and $f \leq 0.3$ day^{-1}. Contour interval: (a) 5 m s^{-1}, (b)–(e) 2.5 m s^{-1}. Negative values are shaded. All filters do Fourier transform and the inverse transform where coefficients outside the specified range are set equal to zero. Panels (a)–(d) consist mainly of gravity waves, while (e) consists mainly of Rossby waves (see the text).

Palm (EP) flux mainly with data of period I (westerly shear phase) and period II (easterly shear phase). The EP flux in the log-pressure coordinate is defined as follows, by dividing Eq. (3.5.3) in Andrews et al.(1987) by $\rho_0 a$:

$$\mathbf{F} = [F^{(\varphi)}, F^{(z)}] \equiv \cos\varphi[\overline{u}_z \overline{v'\theta'}/\overline{\theta}_z - \overline{v'u'},$$

$$\{f - (\overline{u}\cos\phi)_\varphi/(a\cos\varphi)\}\overline{v'\theta'}/\overline{\theta}_z - \overline{w'u'}], \quad (1)$$

where the overbar denotes zonal mean, prime deviation from the zonal mean, $z \equiv -H\ln(p/p_0)$ ($H \equiv 7000$ m),

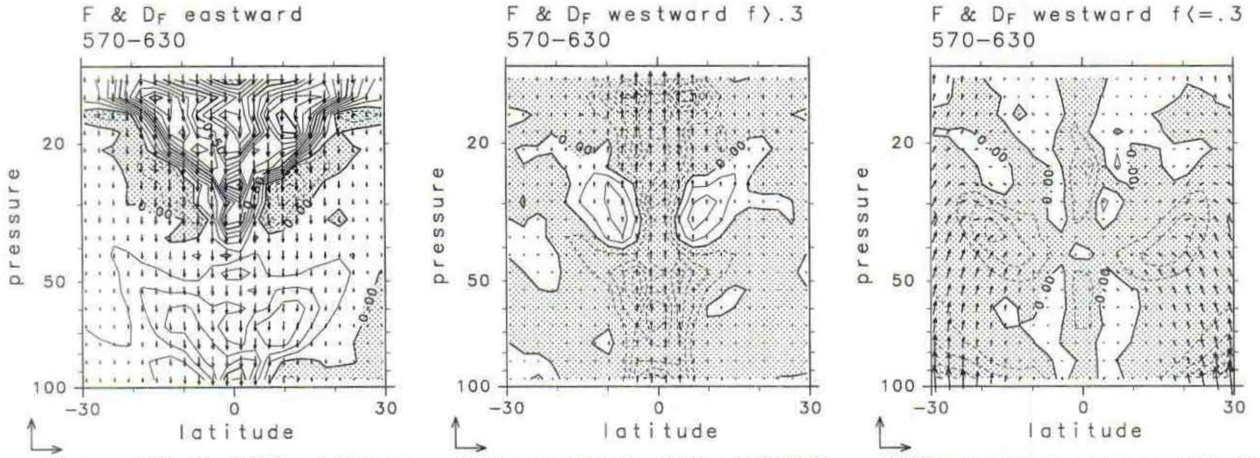

FIG. 13. EP flux **F** (vectors) and its divergence div**F** (contours with interval 0.1 m s^{-1} day^{-1}) averaged over period I. Contributions of eastward-moving disturbances (left), westward-moving disturbances with $f > 0.3$ day^{-1} (middle), and westward-moving disturbances with $f \leq 0.3$ day^{-1} (right). Reference vectors and their magnitudes (m^2 s^{-2}) are shown below each panel, although $F^{(\varphi)}$ is multiplied by a constant so that the direction of the vectors shows that of the wave propagation in the panels.

and others are in standard notation. If $\overline{u}$ and $\overline{\theta}$ are independent of time, zonal wavenumber-frequency distribution of **F** is derived from space–time Fourier coefficients of u', v', w', and θ'. In the following, $\overline{u}$ and $\overline{\theta}$ in Eq. (1) are approximated by their time averages over each of the analyzed periods. We confirmed that errors due to this approximation are small. All variables are interpolated to the log-pressure coordinate to compute **F**.

Figure 13 shows **F** and div**F** averaged over periods I and Fig. 14 for period II. Eastward- and westward-moving components are distinguished using space–time Fourier transform. Furthermore, westward-moving components are divided by frequency in order to distinguish gravity waves ($f > 0.3$ day^{-1}; middle panels) from Rossby waves ($f \leq 0.3$ day^{-1}; right panels). Both eastward- and westward-moving gravity waves (left two panels) have almost vertically oriented EP flux with a maximum over the equator independently of the QBO phase. These results justify the interpretation in terms of meridional modes trapped near the equator as was done in section 4c. On the other hand, Rossby waves in the stratosphere (right panels) propagate from the midlatitude troposphere. Since the midlatitudes of this model are not realistic these waves may not be realistic. However, the contribution of these waves to the QBO-like oscillation is weak since div**F** of these waves is much smaller than that of the westward-propagating gravity waves. Thus, the QBO in this model is driven mainly by gravity waves excited in the low-latitude troposphere.

Period I (Fig. 13) is in a westerly shear phase of the QBO and the eastward acceleration takes place above 40 hPa. In accordance with this, there exists large pos-

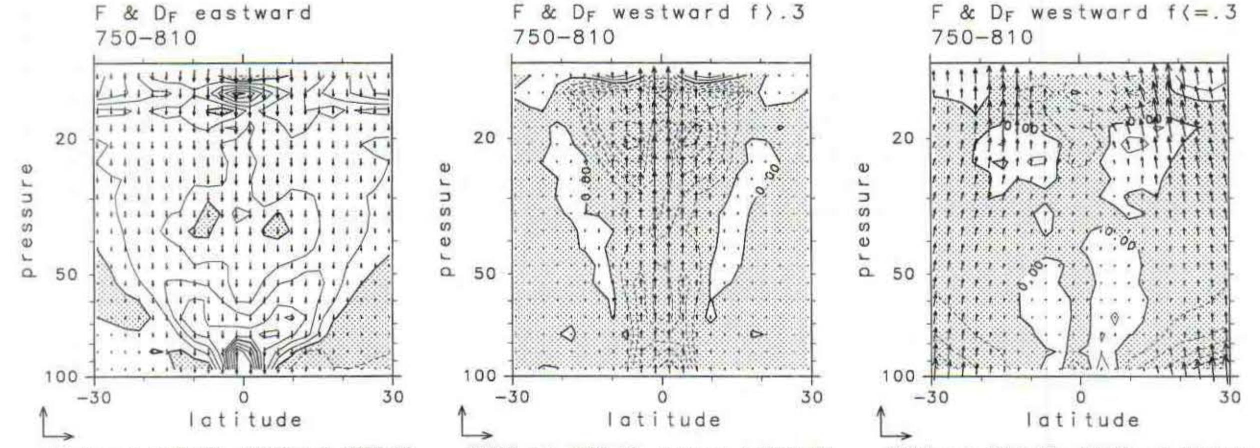

FIG. 14. As in Fig. 13 except for period II.

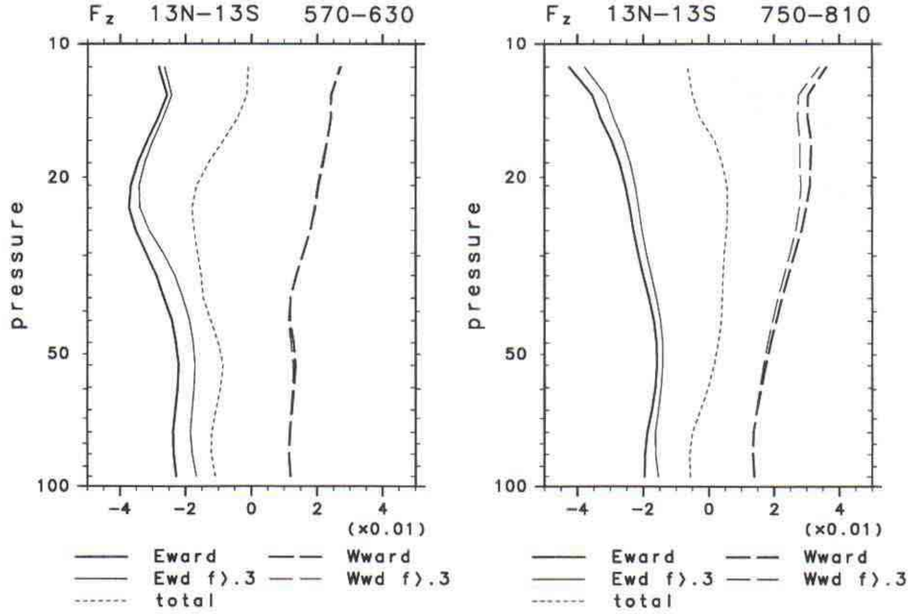

FIG. 15. Vertical component $F^{(z)}$ (m^2 s^{-2}) of the EP flux averaged over $|\varphi| \leq 13°$ for periods I (left) and II (right). Thick solid lines: eastward-moving components, thin solid lines: eastward-moving components with $f > 0.3$ day^{-1}, thick dashed lines: westward-moving components, thin dashed lines: westward-moving components with $f > 0.3$ day^{-1}, and dotted lines: total $F^{(z)}$.

itive div**F** of eastward-propagating gravity waves (the left panel). On the other hand, period II (Fig. 14) is in an easterly shear phase of the QBO and the westward acceleration takes place above 30 hPa. There is large negative div**F** provided by westward-propagating gravity waves (the middle panel).

Figure 15 shows $F^{(z)}$ averaged over $|\varphi| \leq 13°$. Most of it is due to waves having frequencies larger than 0.3 day^{-1} as shown by thin lines. The results are compared with the indirect estimates of $\overline{u'w'}$ by SD97, where contributions of eastward- and westward-moving disturbance were estimated separately for the first time as a study by radiosonde data. They showed that both of the eastward- and westward-moving components have similar magnitude and consist mainly of waves having periods less than 3 days in the westerly shear, $|\overline{u'w'}|_{\text{eastward}} + |\overline{u'w'}|_{\text{westward}}$ is 20–60 × 10^{-3} m^2 s^{-2} with a little excess of the eastward momentum flux, while in the easterly shear it is 7–30 × 10^{-3} m^2 s^{-2} with comparable contribution from both directions. Our results in Fig. 15 show similar imbalance for the westerly shear (period I) and similar balance for the easterly shear (period II). The magnitude of $|F^{(z)}|$ in the westerly shear is in the range of their estimates and that in the easterly shear is about twice the estimates.

Zonal wavenumber distributions of $F^{(z)}$ are summarized in Tables 1 and 2. About 45% of $F^{(z)}$ of eastward-moving disturbances is distributed to s = 4–11 when propagating into the stratosphere (see rows for 95 hPa), and about 40% to $s > 12$. That of westward-moving disturbances is distributed to even higher wavenumbers. In general, as shown by Eq. (B4), $F^{(z)}$ is distributed to larger zonal wavenumbers than wave energy due to the factor s (see also Bergman and Salby 1994).

Figure 16 shows $\langle F^{(z)} \rangle$ of each gravity mode for period II, where $\langle F^{(z)} \rangle$ is defined by Eq. (B5) and is approximately equal to meridionally averaged $F^{(z)}$. For both eastward- and westward-propagating components, the dominant mode is the gravest symmetric mode: Kelvin waves ($n = -1$) for eastward-propagating components and $n = 1$ gravity waves for westward-propagating ones. Contributions of antisymmetric modes are small. The contribution of Kelvin waves in $\langle F^{(z)} \rangle$ of eastward-propagating gravity waves is summarized in Table 3. More

TABLE 1. Zonal wavenumber distributions of $F^{(z)}$ of eastward-moving disturbances (10^{-2} m^2 s^{-2}) averaged over $|\varphi| \leq 13°$ for periods I and II.

		s = 1–3	s = 4–11	s = 12–30	s = 1–42
I	95 hPa	−0.36 (16%)	−1.00 (44%)	−0.85 (37%)	−2.29
	23 hPa	−0.54 (14%)	−1.92 (52%)	−1.22 (33%)	−3.73
II	95 hPa	−0.32 (16%)	−0.88 (45%)	−0.70 (36%)	−1.96
	23 hPa	−0.40 (17%)	−1.30 (54%)	−0.67 (28%)	−2.41

TABLE 2. As in Table 1 except for westward-moving disturbances whose frequencies are larger than 0.3 day^{-1}.

		s = 1–3	s = 4–11	s = 12–30	s = 1–42
I	95 hPa	0.14 (12%)	0.51 (43%)	0.48 (41%)	1.17
	23 hPa	0.42 (22%)	1.01 (51%)	0.50 (26%)	1.96
II	95 hPa	0.11 (8%)	0.63 (46%)	0.57 (41%)	1.37
	23 hPa	0.19 (7%)	1.35 (49%)	1.17 (42%)	2.76

than half of $\langle F^{(z)}\rangle$ of eastward-propagating gravity waves propagating into the stratosphere (see rows for 95 hPa) is due to Kelvin waves. The contribution decreases with s from 80% for $s = 1$–3 to 40% for $s = 12$–30. Note that Kelvin waves of $s > 4$, which are important for the momentum transport, should be interpreted merely as the gravest symmetric gravity modes since the frequency separation from other inertia–gravity waves is small. The contribution of $n = 1$ gravity waves is also summarized in Table 4; more than half of $\langle F^{(z)}\rangle$ is dominated by them and the dependence on s is rather small.

Linear plotting with n as in Fig. 16 may not reflect the meridional mode-number distribution properly since in such a figure all n's are weighted equally. Thus, we tested a pseudo-energy-content view by multiplying $\langle F^{(z)}\rangle$ by $(n + 2)$. Even with the weight, $|\langle F^{(z)}\rangle|$ of symmetric modes decreases with n both for eastward- and westward-propagating gravity waves. Therefore, we can conclude that the meridional mode-number distribution of $\langle F^{(z)}\rangle$ is "red"; the simpler the meridional structure of a mode is, the more significant it is for $\langle F^{(z)}\rangle$.

Figure 17 shows zonal wavenumber-frequency distributions of $F^{(z)}$ and div**F** at 23 hPa averaged over $|\varphi| \leq 13°$ in the energy content form for period I (the upper half) and period II (the lower half). Compared with kinetic energy shown in Fig. 9, $|F^{(z)}|$ and |div**F**| are dominant at higher wavenumbers and frequencies. Signs of $F^{(z)}$ are consistent with upward propagation of wave activity. Although the wavenumber-frequency distributions of div**F** are dappled, their signs on the average indicate that zonal momentum is deposited as waves propagate upward. In period I, during which zonal wind is accelerated eastward at this height, there is large positive div**F** for $20 < c < 40$ m s^{-1} (c: zonal phase velocity), although the phase velocity dominant for $F^{(z)}$ is larger. This implies that eastward-propagating waves with $20 < c < 40$ m s^{-1} are damped around this height and cause the zonal acceleration. These waves consist mainly of Kelvin waves; the Hough-mode expansion of $F^{(z)}$ shows that about 60% of positive div**F** between 47 hPa and 23 hPa in this period is provided by Kelvin waves. In period II during which westward acceleration takes place, on the other hand, there is large negative div**F** of westward-propagating waves around $f \approx 0.8$ day^{-1} and $s \approx 8$. This is mainly due to symmetric gravity waves with small n's; the Hough-mode expansion of $F^{(z)}$ shows that about 50% of negative div**F** between 47 hPa and 23 hPa in this period is provided by $n = 1$ gravity waves.

Divergence of **F**, which contributes to the acceleration of the QBO-like oscillation is distributed over a wide range of zonal wavenumbers from 2 to 30 both for westward and eastward accelerations and the contribution of wavenumber 1 is small. Table 5 summarizes the wavenumber distributions of div**F** associated with the acceleration. The upper row shows the distribution for period I. Eastward-propagating waves with $s = 1$–3 provide only 20% of div**F**, although this percentage is larger than that for $F^{(z)}$ listed in Table 1. Thus, the Kelvin wave of $s = 1$, which is assumed as the carrier of eastward momentum in the theoretical model by Holton and Lindzen (1972) plays only a minor role in this model. On the other hand, the percentage of $s = 4$–11 and $s = 12$–30 is about 50% and 30%, respectively. Thus,

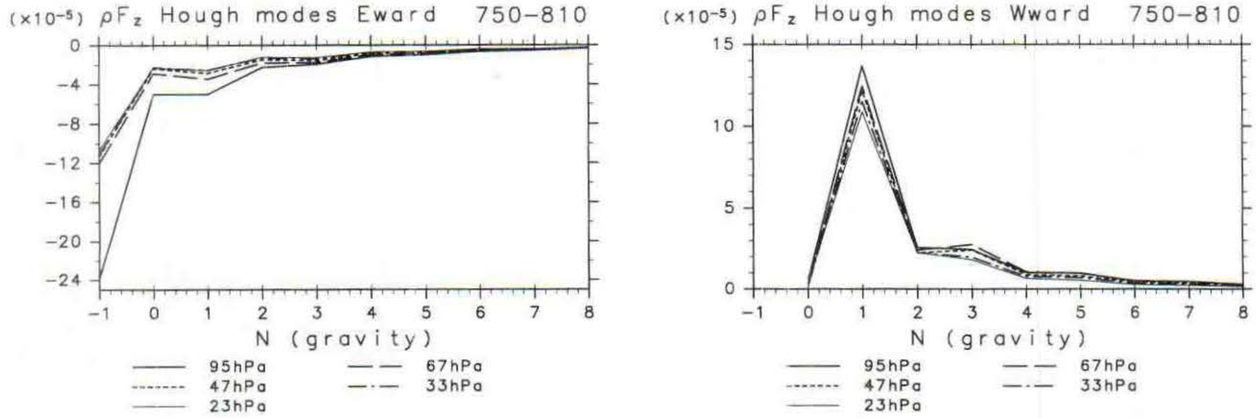

FIG. 16. As in Fig. 11 except for showing $\langle F^{(z)}\rangle$ (m^2 s^{-2}) where eastward- and westward-moving modes are distinguished.

TABLE 3. Percentage of the contribution of the Kelvin waves in $\langle F^{(z)} \rangle$ of eastward-propagating gravity waves with the meridional mode number $n \leq 18$ for the period II.

	$s = 1$–3	$s = 4$–11	$s = 12$–30	$s = 1$–30
95 hPa	79%	63%	42%	57%
23 hPa	66%	60%	32%	51%

TABLE 4. As in Table 3 except for $n = 1$ gravity waves in westward-propagating gravity waves.

	$s = 1$–3	$s = 4$–11	$s = 12$–30	$s = 1$–30
95 hPa	59%	63%	54%	59%
23 hPa	59%	63%	60%	61%

most of the eastward momentum is transported by intermediate-scale gravity (Kelvin and inertia–gravity) waves. The westward acceleration in period II is provided by waves of larger wavenumbers than the eastward acceleration. The contribution of waves with $s = 1$–3 is about 15%, while that of both $s = 4$–11 and $s = 12$–30 is about 40%.

Table 6 shows the frequency distributions of div**F** associated with the acceleration. More than half of the div**F** is provided by waves with $0.3 < f < 1$ (day^{-1}) both for the eastward and westward accelerations; the remaining part of it is distributed mainly to lower frequencies for the eastward acceleration (I), whereas it is distributed mainly to higher frequencies for the westward acceleration (II).

Although descriptions above are based on the classification in terms of zonal wavenumber and frequency, it is more informative to show the phase-velocity distributions of **F** and div**F** in order to compare the results with theories of the QBO. Figure 18 shows vertical sections of zonal phase-velocity distributions of $F^{(z)}$ as well as the zonal-mean zonal winds near the equator for four 60-day periods. For all the periods shown, eastward-moving components have narrower phase-velocity distributions and smaller mean phase velocities than westward-moving ones. The eastward-moving components around 100 hPa have a maximum at 20 m s^{-1} and a secondary peak at 40 m s^{-1}. The westward-moving ones also have local maxima at 20 and 40 m s^{-1}, although the maximum at 20 m s^{-1} is not so conspicuous as that of the eastward-moving ones. The two maxima of eastward-moving components correspond to the two dominant equivalent depths described in section 4c; zonal phase velocity of Kelvin waves is 22 m s^{-1} for $h = 50$ m and 44 m s^{-1} for $h = 200$ m. Note that each panel of Fig. 18 shows that waves having critical levels are damped near their critical levels.

Figure 19 shows vertical sections of phase-velocity distributions of div**F** as well as the zonal-mean zonal wind near the equator. The distributions are narrower than those of $F^{(z)}$, because waves with large intrinsic phase velocities have large vertical group velocities and thus do not suffer significant damping during their vertical propagation. Although a considerable portion of $F^{(z)}$ is distributed to phase velocities larger than 40 m s^{-1}, the divergence is small for such phase velocities. On the other hand, waves having small phase speeds provide div**F** effectively. Especially, waves having critical levels provide large |div**F**| near their critical levels, although $F^{(z)}$ of such waves is not always large. Vertical averages of div**F** over 70–15 hPa (not shown) are distributed to phase speeds mainly over 10–40 m s^{-1} with a maximum at 20 m s^{-1} both for eastward- and westward-moving components. The phase-velocity distribution of div**F** contributing to the QBO-like oscillation is summarized in Table 7 in terms of the intrinsic phase velocity $(c - U)$. Waves with $|c - U| < 10$ m s^{-1} provide 30%–50% of div**F** driving the oscillation, while the contribution of waves with $|c - U| > 20$ m s^{-1} is small.

6. Discussion

a. *Effect of the Brewer–Dobson circulation*

Dunkerton (1991) pointed out that the equatorial upwelling of the Brewer–Dobson circulation acts to hinder the downward propagation of the QBO phases (see Dunkerton 1997 for a review). Recent observations of water vapor in the equatorial lower stratosphere (Mote et al. 1996) show that the upwelling in this region has about the same speed as that of the downward propagation of the QBO phases. Thus, about half of the momentum deposition by waves is consumed in sustaining the QBO phases against the upwelling.

Our model has almost no Brewer–Dobson circulation since planetary waves in mid- and high latitudes are very weak because of the absence of mountains and jet streams. Thus, if a realistic equatorial upwelling existed in the model, the period of the QBO-like oscillation might be doubled since the downward propagation of the QBO phases would be halved. If so, the period of the oscillation becomes about 800 days, which is close to the period of the QBO in the real atmosphere.

b. *Phase velocities of waves contributing to the QBO acceleration and their implications for the vertical resolution for the simulation of the QBO*

Waves contributing to the acceleration of the QBO-like oscillation in this model are gravity waves with various scales from planetary to intermediate scales. As shown in Figs. 18 and 19, the phase velocities of the waves are distributed continuously and a considerable portion of the acceleration of the QBO-like oscillation is provided by waves having a critical level. These results suggest that waves contributing to the oscillation are something like those assumed by Lindzen and Holton (1968), who considered gravity waves with continuous phase-velocity distributions, rather than those assumed by Holton and Lindzen (1972), who considered

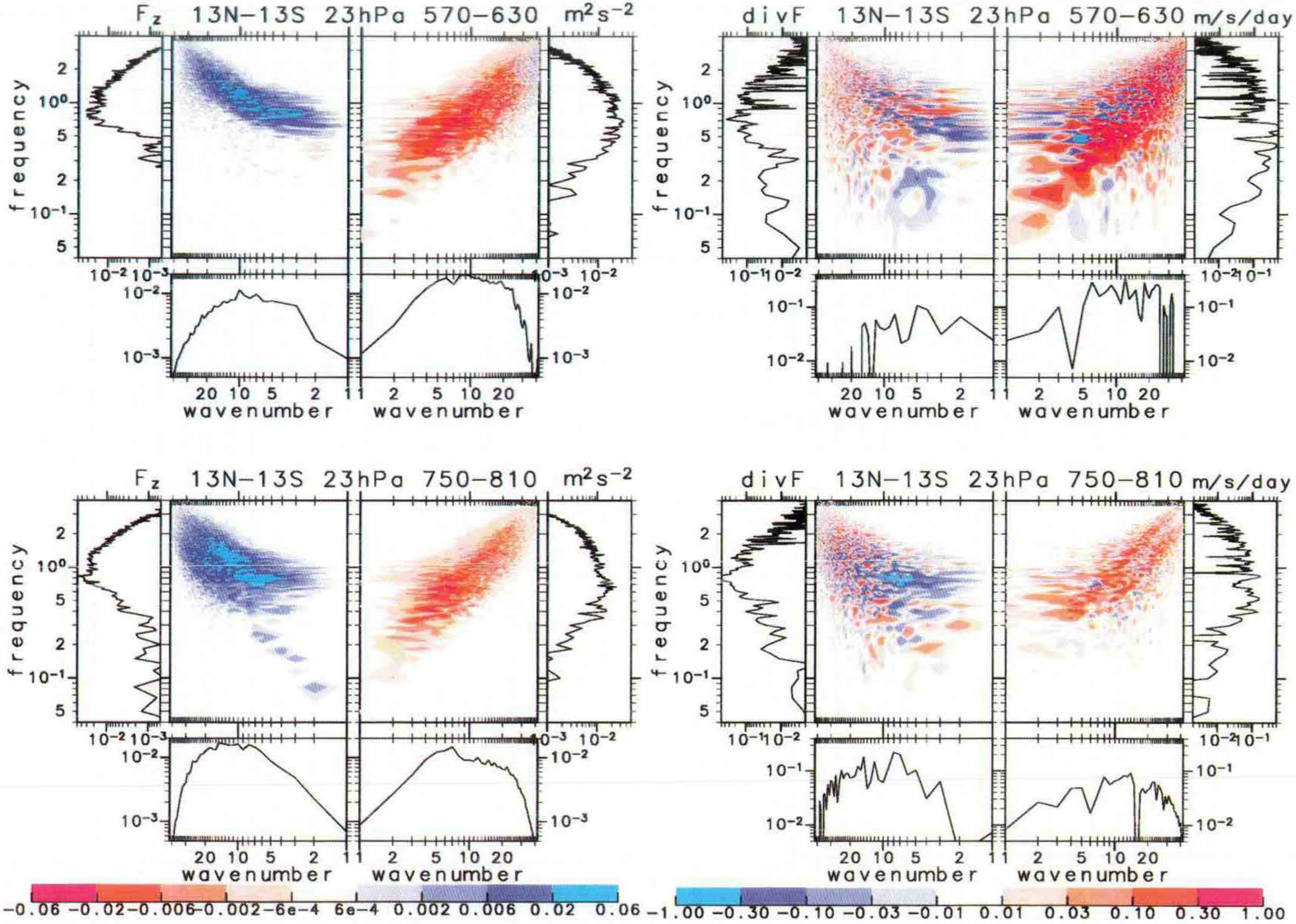

FIG. 17. As in Fig. 9 except for showing $F^{(z)}$ at 23 hPa (m^2 s^{-2}) (left panels) and div**F** (m s^{-1} day^{-1}) (right panels) averaged over $|\varphi| \le 13°$. The upper half is for period I and the lower half for period II. For div**F**, the three-point smoothing (appendix A) is done with respect to frequency.

TABLE 5. Zonal wavenumber distributions of div**F** (0.1 m s^{-1} day^{-1}) of eastward-moving disturbances averaged over $|\varphi| \le 13°$ and 33–15 hPa for period I (the first row), and those of westward-moving disturbances averaged over $|\varphi| \le 13°$ and 26–13 hPa for period II (the second row). These pressure bounds correspond to the heights where the zonal wind is accelerated intensively.

	s = 1–3	s = 4–11	s = 12–30	s = 1–42
I: eastward-propagating waves	0.68 (19%)	1.75 (48%)	1.17 (32%)	3.63
II: westward-propagating waves	−0.42 (14%)	−1.30 (43%)	−1.19 (40%)	−2.97

two planetary-scale waves with discrete phase velocities without any critical level.

The divergence of zonal momentum flux in low latitudes is distributed to phase speeds over 10–40 m s^{-1} with a characteristic phase speed of 20 m s^{-1}. Some 30%–50% of momentum flux deposition is distributed to intrinsic phase speeds less than 10 m s^{-1}. Such slow waves have small vertical wavelengths. Moreover, waves approaching the critical level reduce their vertical wavelengths. Now we can roughly estimate the vertical resolution required to simulate the momentum transport and deposition by these waves. If we assume Kelvin waves or small-scale gravity waves free from the effect of earth's rotation (this is a good assumption for gravity waves of large wavenumber), the vertical wavelength $\lambda_z = (2\pi/N)|c - U| = (2\pi/N)(gh)^{1/2}$. Thus, $\lambda_z = 5.7$ km for $|c - U| = 20$ m s^{-1} and $\lambda_z = 2.9$ km for $|c - U| = 10$ m s^{-1} if $N = 2.2 \times 10^{-2}$ s^{-1}. These values are consistent with the time–height sections of wave disturbances shown in Fig. 12. Boville and Randel (1992) showed that vertical grid spacings of 1 km or less are required in order to simulate div**F** of RG waves with $\lambda_z \approx 5$ km properly. Thus, in order to simulate div**F** of gravity waves with $|c - U| \approx 10$ m s^{-1}, vertical grid spaings as small as about 500 m appear to be required. The vertical grid spacing of this model is about 700 m and it seems to be close to a marginal value to simulate div**F**. Moreover, since there are some observational evidences that gravity waves with $\lambda_z = 2$–3 km exist in the equatorial lower stratosphere (e.g., Tsuda et al. 1994b), vertical grid spacings smaller than 700 m appear to be preferable to simulate the effect of these waves in order to simulate the QBO.

c. *Horizontal diffusion*

To simulate the QBO with a T21 comprehensive GCM, Takahashi (1996) had to change two standard parameters. One is to reduce the vertical grid spacing, the necessity of which was already discussed. The other is to reduce the coefficients of horizontal diffusion by more than one order of magnitude. However, the necessity of this is not clear.

Generally horizontal diffusion is incorporated in spectral models in order to prevent energy accumulation at large wavenumbers. It is not determined physically but numerically; the coefficients of the diffusion are usually expressed in terms of the *e*-folding time at the maximum total wavenumber and typically given by a value of about a day or less. The "standard" diffusion determined in this way for T21 rapidly damps intermediate-scale waves, which seem to be important for the QBO acceleration, much more effectively than radiative processes do. That is, such a "standard" horizontal diffusion in the models with T21 or lower resolution is too large to simulate the momentum transport contributing to the QBO.

The coefficients of the horizontal diffusion in our model, which produces a quite realistic QBO-like oscillation, are standard ones. However, since the resolution is T42 and a hyperdiffusion proportional to ∇^6 is used instead of ∇^4 by Takahashi (1996), it does not damp most of the intermediate-scale waves much; the damping rate is comparable or smaller than that of Newtonian cooling for wavenumbers smaller than 20 (see section 6d).

This discussion implies that the reduction of horizontal diffusion is necessary only for low-resolution models such as T21 and is not a necessary condition for the simulation of the QBO, while a fine vertical grid spacing appears to be necessary.

d. *Wave damping in the model*

Several processes that cause wave damping in the model are classified into linear and nonlinear ones. The linear processes consist of horizontal and vertical diffusions and Newtonian cooling; the Rayleigh friction is incorporated only in the sponge layer. The *e*-folding time of Newtonian cooling is set equal to 20 days. The horizontal diffusion has the same damping rate as Newtonian cooling at horizontal total wavenumber 20 and the vertical diffusion has the same damping rate at vertical wavelength 3.7 km. Here, we estimated the scales corresponding to an *e*-folding time of 40 days taking it into account that Newtonian cooling damps only tem-

TABLE 6. As in Table 5 except for showing the frequency distributions. The unit of the frequency f is cycles per day.

	$f \le 0.1$	$0.1 < f \le 0.3$	$0.3 < f \le 1$	$1 < f$	Total
I: eastward-propagating waves	0.29 (8%)	0.97 (27%)	1.93 (53%)	0.44 (12%)	3.63
II: westward-propagating waves	−0.19 (6%)	−0.20 (7%)	−1.76 (59%)	−0.82 (28%)	−2.97

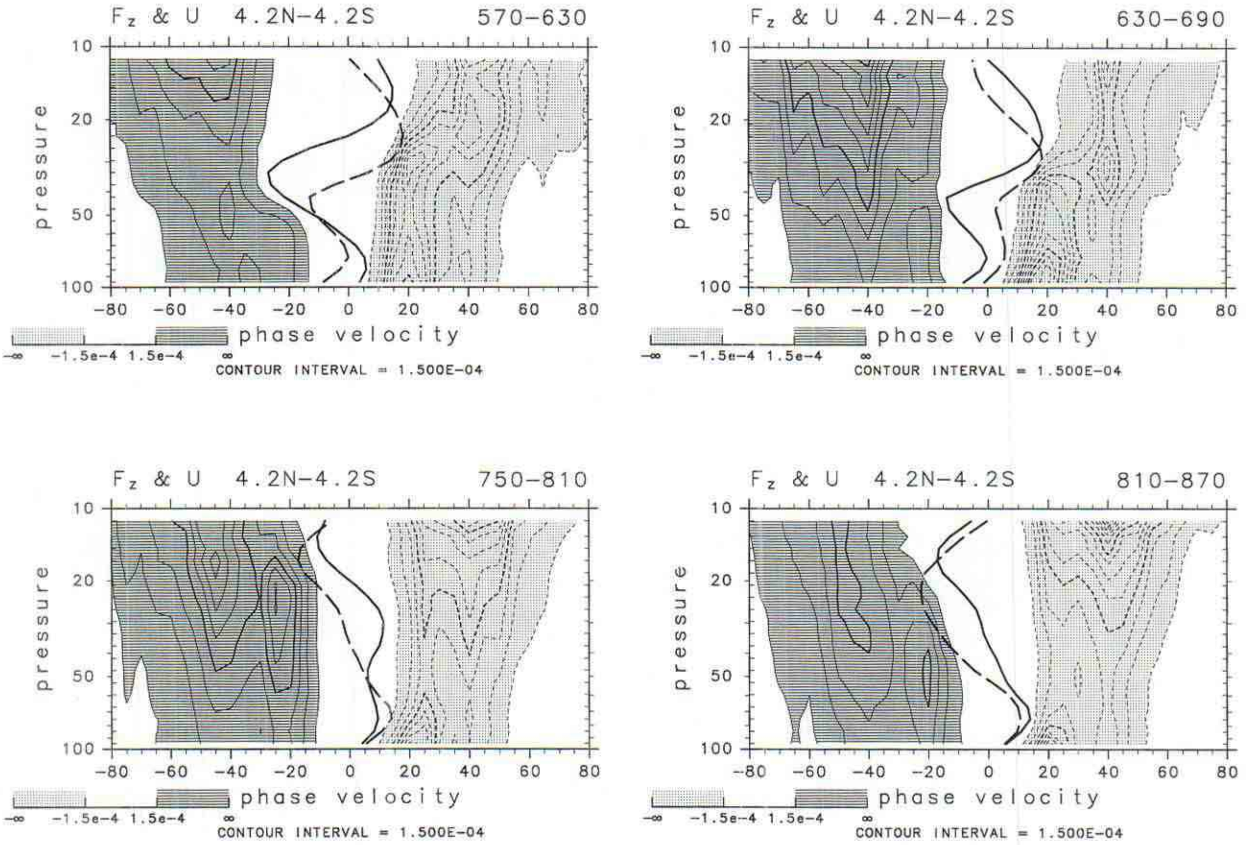

FIG. 18. Zonal phase velocity–height distributions of $F^{(z)}$ [m s^{-1} = m^2 s^{-2}/(m s^{-1})] averaged over $|\varphi| \leq 4.2°$ for four 60-day periods: days 570–630 of period I, 630–690 and 750–810 of period II, and 810–870. No zero contours are shown. Thick solid lines show zonal-mean zonal wind averaged over $|\varphi| \leq 4.2°$ at the beginning of each period and thick dashed lines show that at the end of the period.

perature disturbances. Most of the momentum transport contributing to the QBO acceleration is distributed to larger scales than these. Thus, the dominant linear damping process in this model is Newtonian cooling. However, the diffusion is not negligible. Especially, the vertical diffusion may be significant for the damping in the vicinity of critical levels.

Radiative processes in the stratosphere can be well approximated by Newtonian cooling whose coefficient is dependent on vertical wavelength and height (Fels 1982). The damping timescales are smaller for smaller vertical wavelengths (λ_z) and higher altitudes. According to his estimates, the *e*-folding time for waves with λ_z = 6 km is 10 days at 20 km and 5 days at 30 km, both of which are smaller than that used in this model (20 days). This value is comparable to the *e*-folding time of waves with λ_z = 12 km at 20 km. Thus, if we incorporate a realistic radiative scheme into the model, waves with small vertical wavelengths will be damped more effectively. It is of interest how the QBO-like oscillation will be changed by this improvement.

The nonlinear damping processes include wave–wave interaction and wave breaking. The latter is parameterized by the dry convective adjustment, which is examined here. Figure 20 shows the magnitude of the dry convective adjustment and Newtonian cooling over the equator. The magnitude of Newtonian cooling is in 0.1–0.2 K day^{-1} in most of the region shown in the figure. It is sometimes larger than 0.2 K day^{-1} between 13 and 20 hPa and along the lines where zonal wind is nearly equal to zero in the westerly shear of the QBO (see Fig. 5), but never exceeds 0.3 K day^{-1}. On the other hand, the magnitude of the dry convective adjustment varies much larger; in most regions shown in the figure it is less than 0.02 K day^{-1}, but it exceeds 0.3 up to about 1 K day^{-1} in the vicinity of the zero-wind lines in the westerly shear. Thus, Newtonian cooling is the dominant damping process except for the westerly shear zones.

The reason why the wave breaking is confined in the vicinity of the zero-wind lines in the westerly shear seems to be that the amplitude of the eastward-propagating waves is larger than that of the westward-propagating ones and that dispersion of the former waves, which consist mainly of Kelvin waves, is smaller.

e. Waves contributing to the QBO

Waves in the equatorial lower stratosphere in our model seem to have greater energy than in the real atmosphere (section 4b) and their momentum flux is a

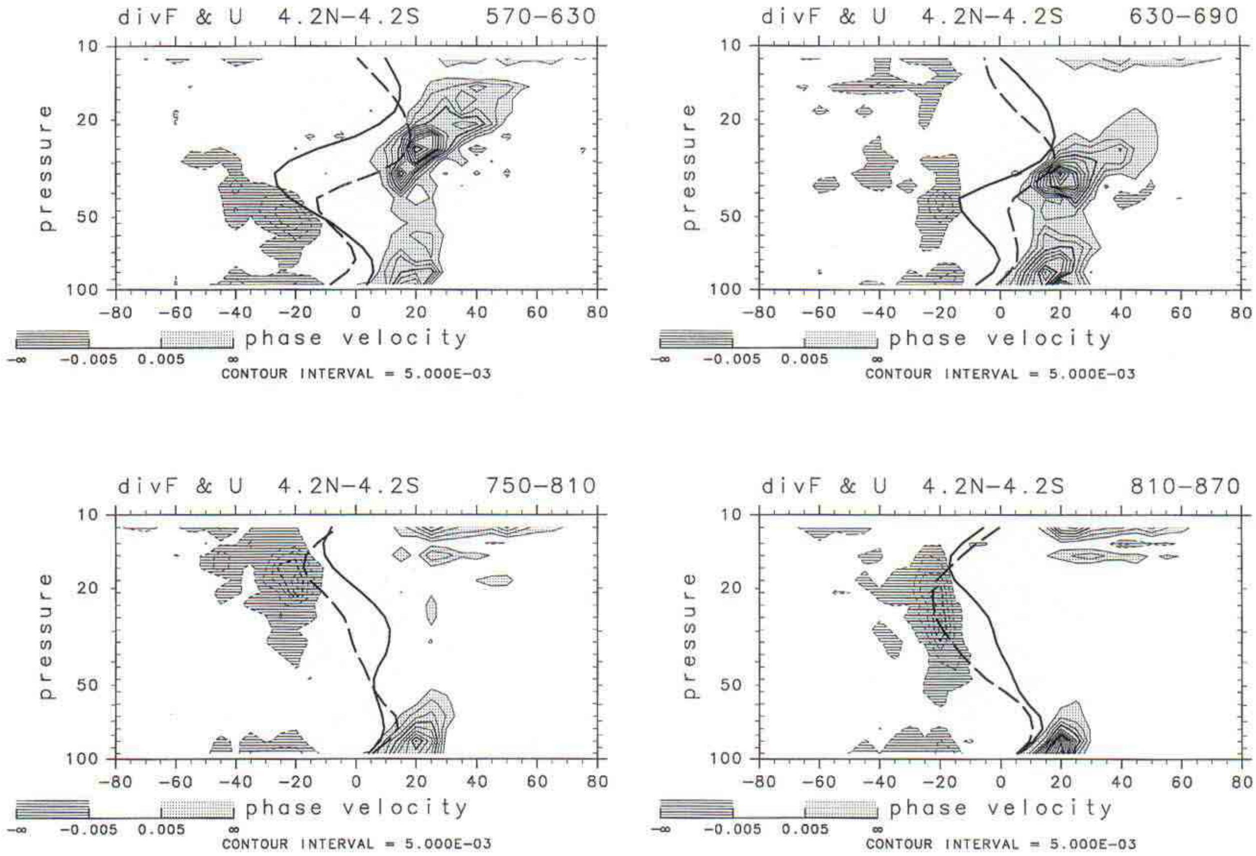
divF & U 4.2N–4.2S 570–630

divF & U 4.2N–4.2S 630–690

divF & U 4.2N–4.2S 750–810

divF & U 4.2N–4.2S 810–870

FIG. 19. As in Fig. 18 except for div**F** (day^{-1}).

little larger than the indirect estimates by SD97 (section 6), although observations are still not enough to estimate the entire spectrum of waves in the equatorial stratosphere. Now suppose that the momentum flux in the model is realistic and the wave energy in the model is larger than in the real atmosphere. This indicates that the ratio of $|u'|$ to $|w'|$, or the phase tilts of waves, in the model is larger than in the real atmosphere on an average, since the ratio of $\overline{u'^2}$ (approximately proportional to the energy) to $\overline{u'w'}$ (approximately proportional to the momentum flux) is larger. This implies that the horizontal scales of waves in the model are larger than in the real atmosphere since the vertical scales seem to be comparable while phase tilts are smaller. In fact, the horizontal resolution of T42 is not enough to cover the broad wavenumber distribution suggested by Bergman and Salby (1994) and is not enough to resolve the cloud clusters with horizontal scales about 100 km. Although waves with small horizontal scales have large vertical group velocities, they will be damped even in the lower stratosphere if they have critical levels. Pfister et al. (1993a,b) reported quasi-stationary mesoscale gravity waves excited by tropical mesoscale convection. As they estimated, such mesoscale gravity waves may supplement the QBO acceleration in the real atmosphere.

TABLE 7. Distributions of div**F** in terms of intrinsic zonal phase velocities. Here, div**F** of eastward-moving (upper two rows) or westward-moving (lower two rows) disturbances is averaged over $|\varphi| \le 4.2°$ for four periods. For each period, three pressure levels centered at the level where total div**F** of eastward- or westward-moving disturbances is maximum are selected as listed in the second column. Divergence of **F** is summed up for three ranges with respect to $c - U$ (m s^{-1}) shown in the table, where c is the phase velocity and U is mean zonal wind at each level averaged over the period and $|\varphi| \le -4.2°$. Only the percentage is listed in the table.

Period	Pressure levels	$0 < c - \mathrm{U} < 10$	$10 < c - U < 20$	$20 < c - U$
570–630 days (I)	26.3–20.8 (hPa)	27%	58%	15%
630–690 days	37.4–29.6 (hPa)	36%	45%	19%
		$-10 < c - U < 0$	$-20 < c - U < -10$	$c - U < -20$
750–810 days (II)	18.5–14.7 (hPa)	30%	32%	38%
810–870 days	29.6–23.4 (hPa)	51%	24%	25%

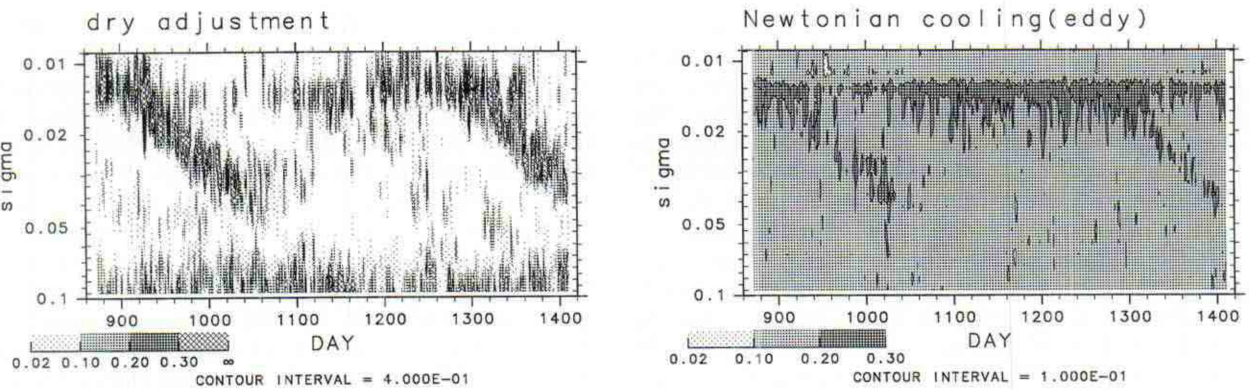

FIG. 20. Time–height sections of zonally averaged absolute values of dry convective adjustment (left) and Newtonian cooling for the temperature deviation from the zonal mean (right). The unit is K day^{-1}. Note that the contour intervals and shading are not the same for these two panels.

f. Rossby–gravity waves

In this model, the EP flux due to westward-propagating RG waves is much smaller than that due to westward-propagating $n = 1$ gravity waves. The amplitude of the RG waves seems to be smaller than that observed in the real atmosphere too. Although the direct estimation with a Fourier filter is difficult because of the presence of Rossby waves, a rough estimation from the kinetic energy derived by the Hough-mode expansion suggests that the amplitude of the meridional wind associated with westward-propagating RG waves of zonal wavenumbers 3–6 is about 1 m s^{-1}. This is smaller than the typical observed value of 2–3 m s^{-1}.

Since the "ITCZ" in this model is over the equator, it is natural to expect that RG waves are weak; Hess et al. (1993) conducted aquaplanet simulations with various combinations of cumulus parameterizations and SST distributions and showed that RG waves are active when a model has two ITCZs straddling the equator. In addition, RG waves in our model may be weak because midlatitude processes are not realistic due to the assumption of constant SST; there are observational evidences that westward-propagating RG waves are excited or triggered by forcing from midlatitudes (see Magaña and Yanai 1995).

g. Asymmetry between easterly and westerly flows in the QBO

In the QBO-like oscillation, the maximum speed of easterly wind is larger than that of the westerly wind, as in the QBO of the real atmosphere. This may be because westward momentum flux in the equatorial lower stratosphere is distributed to larger phase speeds than the eastward one (Fig. 18) and thus the westward-propagating waves have larger "effective phase speeds" than the eastward-propagating waves (Saravanan 1990). The westward-propagating gravity waves have larger phase speeds than Kelvin waves especially at small wavenumbers. Taking these into account, it seems reasonable that the QBO-like oscillation obtained by Takahashi and Shiobara (1995) with a 1/5 sector model with T106 resolution has larger maximum westerly wind than maximum easterly wind since their model does not contain zonal wavenumbers less than 5. However, it is not explained from this point of view why the full spherical model with T21 resolution used by Takahashi (1996) also produced faster westerly wind. This could be because the tropical cumulus convection in his model is not very realistic (Takahashi et al. 1997).

As shown in section 3b, the eastward acceleration of the QBO-like oscillation is larger than the westward acceleration as in the real atmosphere. This asymmetry was explained first by Plumb and Bell (1982) in terms of the asymmetry of the meridional circulation that accompanies the QBO. In the present model, the meridional residual circulation contributes to the asymmetry of the acceleration too (not shown). However, the asymmetry of div**F** itself contributes more to the asymmetry of the acceleration.

h. Semiannual oscillation as an upper boundary condition

The semiannual oscillation in the real atmosphere may help the evolution of the QBO by producing critical levels (e.g., Lindzen and Holton 1968; Takahashi 1996). Our model does not have the semiannual oscillation. Instead, zonal-mean wind above 10 hPa is kept to almost zero by the Rayleigh friction. Thus, the upper boundary condition of the present model does not promote the QBO-like oscillation.

7. Conclusions

A QBO-like oscillation is obtained with a simplified GCM and the wave–mean flow interaction associated with the oscillation is investigated. Although the SST is uniform in this model, the Hadley circulation exists in low latitudes and cumulus convection near the equator is separated from that in mid- and high latitudes. The cumulus convection in low latitudes has realistic hierarchy that small-scale westward-moving structures exist in large-scale eastward-moving structures. The model reproduced the observed large-scale organization of cumulus convection along the dispersion curves of equatorial waves with equivalent depths about 20 m.

The QBO-like oscillation produced in the model has a period of about 400 days. However, if a realistic magnitude of the equatorial upwelling of the Brewer–Dobson circulation is incorporated, the period is may be doubled, thus nearly equal to that of the QBO in the real atmosphere. The peak eastward mean flow accelerations are larger than the peak westward accelerations and the downward propagation of the westerly shear zones is faster than that of the easterly shear zones. The meridional width of the oscillation is also realistic and the transition to the westerly begins within narrower meridional extent than that to the easterly. The maximum easterly wind speed is 28 m $\mathrm{s^{-1}}$ and is larger than the maximum westerly wind speed of 22 m $\mathrm{s^{-1}}$. All of these features show that the QBO-like oscillation in this model is quite realistic. This is the first simulation with a GCM that reproduced the observed asymmetry of the maximum zonal wind speeds.

Waves in the equatorial lower stratosphere of the model are excited mainly by cumulus convection in low latitudes. Since the cumulus convection has some realistic features, these waves are also expected to have some realistic features. Most of the energy and EP flux of these waves is due to gravity waves including Kelvin waves. Although Rossby waves propagate from midlatitudes, they are not significant for the acceleration of the QBO-like oscillation. The energy of the gravity waves is distributed to zonal wavenumbers 1–20. The vertical component of the EP flux is distributed to even higher zonal wavenumbers (thus to higher frequencies) as is naturally expected; most of the EP flux is due to intermediate-scale waves with higher frequencies than 0.3 $\mathrm{day^{-1}}$.

The gravity waves can be interpreted in terms of meridional modes trapped near the equator. The dominant waves in the stratosphere are gravity waves having equivalent depths about 40–100 m or 200 m; the smaller characteristic equivalent depths increase with height while the larger one is roughly constant. More than half of the westward momentum flux propagating into the stratosphere is due to Kelvin waves, while more than half of the eastward momentum flux is due to $n = 1$ gravity waves. Note that Kelvin waves with zonal wavenumber larger than 4, which are important for the momentum transport, should be interpreted merely as the gravest symmetric gravity modes since the frequency separation from other inertia–gravity waves is small. Antisymmetric modes such as Rossby–gravity waves are weak in this model, and dependence of zonal momentum flux on the meridional mode number n is "red."

Divergence of the EP flux, which contributes to the acceleration of the QBO-like oscillation, is distributed over the wide range of zonal wavenumbers from 2 to 30. About 20% of the divergence of eastward momentum flux contributing to the eastward acceleration is distributed to wavenumbers 1–3, about 50% to 4–11, and about 30% to more than 12. The divergence of westward momentum flux contributing to the westward acceleration is distributed to even higher wavenumbers: 15% to 1–3, 45% to 4–11, and 40% to more than 12. These results support the significance of short-period gravity waves with intermediate scales, as is suggested observationally and theoretically (e.g., Sato and Dunkerton 1997; Dunkerton 1997). As for meridional modes, about half of the divergence, as well as the momentum flux itself, is due to Kelvin waves (eastward) and westward-propagating $n = 1$ gravity waves (westward).

The vertical component of the EP flux in the equatorial lower stratosphere is distributed to phase speeds of 5–80 m $\mathrm{s^{-1}}$, while its divergence contributing to the acceleration of the QBO-like oscillation is to 10–40 m $\mathrm{s^{-1}}$ with a maximum around 20 m $\mathrm{s^{-1}}$. Waves with such small phase speeds often have critical levels and a considerable portion of the acceleration of the QBO-like oscillation is provided by the momentum deposition by gravity waves having critical levels. Thus, the waves contributing to the oscillation are similar to those assumed by Lindzen and Holton (1968) rather than those assumed by Holton and Lindzen (1972). Some 30%–50% of momentum flux deposition is distributed to intrinsic phase speeds less than 10 m $\mathrm{s^{-1}}$. To represent the propagation and damping of the waves with such small intrinsic phase speeds properly in a model, the vertical resolution should be high enough, typically a grid spacing of 500 m. Takahashi (1996) showed that in order to simulate the QBO he had to use such a fine spacing as well as to reduce the horizontal viscosity. The former seems necessary to GCMs in order to simulate the QBO, while the latter seems necessary only to those having low horizontal resolution such as T21.

Acknowledgments. The authors wish to thank Drs. Y. Hayashi and A. Numaguti for their helpful discussions and comments on this work. GFD-DENNOU Library was used for drawing figures and the model used in this study is based on a GCM (AGCM5) in this library. Numerical calculation was done on the SX3 at Computation Center, Osaka University, and on the KDK system at Radio Atmospheric Science Center, Kyoto University. This work was supported in part by the Grant-in-Aid for Scientific Research of the Ministry of Education, Science, Sports and Culture of Japan; and by the Grant-in-Aid for the Cooperative Research with Center for Climate System Research, University of Tokyo.

APPENDIX A

Spectral Analyses and Other Analysis Methods

Spectra in this study are one-sided power spectral densities derived by the direct method with the fast Fourier transform. Thus, the space–time power spectral density of a quantity x is defined as follows (Hayashi 1982):

$$P(s, f) \equiv 2T\,|\tilde{x}(s, f)|^2, \tag{A1}$$

where T (day) is the period analyzed and

$$\tilde{x}(s, f) \equiv \frac{1}{2\pi T}\int_{t_0}^{t_0+T}\int_0^{2\pi} x(\lambda, t)e^{-i(s\lambda-2\pi ft)}\,d\lambda dt. \tag{A2}$$

Here λ, t, s, and f are longitude, time, zonal wavenumber, and frequency, respectively. One-dimensional power spectral densities with respect to zonal wavenumber or frequency are derived by integrating Eq. (A1) with frequency or zonal wavenumber, respectively. When axes are shown in logarithmic scales, an energy content form of the power spectral densities is used:

$$Q(s, f) \equiv 2Tfs|\tilde{x}(s, f)|^2. \tag{A3}$$

The energy content form of one-dimensional power spectral densities is defined in the same way by multiplying by s or f.

When explicitly mentioned in figure captions, spectra are smoothed with a three-point smoothing filter of 1/4: 1/2:1/4.

All interpolations are done with the cubic spline interpolation. This is used for numerical differentiation too.

Meridional averaging in this paper is done with respect to $\sin\varphi$ (φ is latitude) or equivalently with respect to φ with a weight of $\cos\varphi$.

APPENDIX B

Expansion by Hough Functions

The computational methods and validation of the expansion of wave energy and EP flux by Hough modes are described in the following. Hough functions are calculated with expansion by associated Legendre polynomials as eigenvalue problems for given zonal wavenumbers and frequencies. The total wavenumber is truncated at 42 as in the present GCM. Since eigensolutions with small equivalent depths (h) are not accurate due to truncation errors and we are not interested in high latitudes, those solutions with $h < 5$ m are not used. Furthermore, we use data only within $\varphi = \pm 30°$ for the expansion; for gravity modes (Kelvin, RG, and inertia–gravity waves), the results are roughly equal to those without such a meridional cutoff.

Variables necessary for the calculation are interpolated into the log-pressure coordinate. Wave potential energy in the log-pressure coordinate is expressed as follows:

$$P \equiv \frac{1}{2}\overline{(\Phi'_z/N)^2}, \tag{B1}$$

where Φ' is geopotential deviation, subscript z denotes the differentiation by $z \equiv -H\log(p/1000)$, and N is the log-pressure bouyancy frequency. Since Hough functions are eigenfunctions of Φ' and T' (temperature deviation), P of each Hough mode can be derived from both of these, where the vertical structure equations for linearized primitive equations (see Andrews et al. 1987) are assumed in order to differentiate Φ' with z. Since the model is not conservative nor linear with respect to a resting (or rigidly rotating) basic state, expansion by Hough functions is not necessarily meaningful, although it is always possible. To validate the expansion, the two estimates with Φ' and T' are compared with each other since they do not coincide with each other because of these nonconservative and nonlinear effects. As a result, the difference of the two estimates is small for small n's in an appropriate rigidly rotating basic state is incorporated.

In the main text, wave energy is calculated from T', where total energy averaged horizontally over the whole globe is given by

$$\langle E\rangle \equiv \frac{1}{4\pi}\int_{-1}^{1}\int_0^{2\pi}[u'^2 + v'^2 + (\Phi'_z/N)^2]\,d\lambda d(\sin\varphi). \tag{B2}$$

Here, linearized solutions of u' and v' are used. Thus, $\langle E\rangle$ is derived only from T'.

If the disturbances are steady, the vertical component of the EP flux [Eq.(1)] can be expressed as follows under the same assumptions as are necessary for the separation of variables to derive Laplace's tidal equations:

$$F^{(z)} = \Phi'_\lambda\,\Phi'_z/(aN^2), \tag{B3}$$

where a is the earth's radius. For a zonal wavenumber s,

$$F^{(z)} = \mathrm{Re}(is\Phi'\Phi'_z)/(aN^2). \tag{B4}$$

From this equation, it is understood that $F^{(z)}$ is distributed to larger zonal wavenumbers than wave energy in general. Meridionally averaged $F^{(z)}$ of each Hough mode is defined by

$$\langle F^{(z)}\rangle \equiv \frac{1}{4\pi aN^2}\int_{-1}^{1}\int_0^{2\pi}(\Phi'_\lambda\Phi'_z)\,d\lambda d(\sin\varphi), \tag{B5}$$

where N is set to be a function only of z, and the integration in the right-hand side is calculated from the expansion by the Hough function.

REFERENCES

Andrews, D. G., J. R. Holton, and C. B. Leovy, 1987: *Middle Atmosphere Dynamics.* Academic Press, 489 pp.

Bergman, J. W., and M. L. Salby, 1994: Equatorial wave activity derived from fluctuations in observed convection. *J. Atmos. Sci.*, **51,** 3791–3806.

Boville, B. A., and W. J. Randel, 1992: Equatorial waves in a stratospheric GCM: Effects of vertical resolution. *J. Atmos. Sci.*, **49,** 785–801.

Dunkerton, T. J., 1991: Nonlinear propagation of zonal winds in an atmosphere with Newtonian cooling and equatorial wavedriving. *J. Atmos. Sci.*, **48,** 236–263.

——, 1997: The role of gravity waves in the quasi-biennial oscillation. *J. Geophys. Res.*, **102**(D22), 26 053–26 076.

——, and D. P. Delisi, 1985: Climatology of the equatorial lower stratosphere. *J. Atmos. Sci.,* **42,** 376–396.

Fels, S. B., 1982: A parameterization of scale-dependent radiative damping rates in the middle atmosphere. *J. Atmos. Sci.,* **39,** 1141–1152.

Hamilton, K., 1984: Mean wind evolution through the quasi-biennial cycle in the tropical lower stratosphere. *J. Atmos. Sci.,* **41,** 2113–2125.

Hayashi, Y., 1976: Non-singular resonance of equatorial waves under the radiation condition. *J. Atmos. Sci.,* **33,** 183–201.

——, 1982: Space-time spectral analysis and its application to atmospheric waves. *J. Meteor. Soc. Japan,* **60,** 156–171.

——, and D. G. Golder, 1994: Kelvin and mixed Rossby–gravity waves appearing in the GFDL "SKYHI" general circulation model and the FGGE dataset: Implications for their generation mechanism and role in the QBO. *J. Meteor. Soc. Japan,* **72,** 901–935.

——, ——, and J. D. Mahlman, 1984: Stratospheric and mesospheric Kelvin waves simulated by the GFDL "SKYHI" general circulation model. *J. Atmos. Sci.,* **41,** 1971–1984.

Hess, P. G., H. H. Hendon, and D. S. Battisti, 1993: The relationship between mixed Rossby–gravity waves and convection in a general circulation model. *J. Meteor. Soc. Japan,* **71,** 321–338.

Holton, J. R., and R. S. Lindzen, 1972: An updated theory for the quasi-biennial cycle of the tropical stratosphere. *J. Atmos. Sci.,* **29,** 1076–1080.

Horinouchi, T., and S. Yoden, 1996: Wave excitation by localized heating in the tropics and its propagation into the middle atmosphere. *J. Meteor. Soc. Japan,* **74,** 189–210.

Lindzen, R. S., and J. R. Holton, 1968: A theory of the quasi-biennial oscillation. *J. Atmos. Sci.,* **25,** 1095–1107.

——, and C.-Y. Tsay, 1975: Wave structure of the tropical stratosphere over the Marshall Islands area during 1 April–1 July 1958. *J. Atmos. Sci.,* **32,** 2008–2021.

Madden, R. A., and P. R. Julian, 1972: Description of global-scale circulation cells in the tropics with a 40–50 day period. *J. Atmos. Sci.,* **29,** 1109–1123.

Magaña, V., and M. Yanai, 1995: Mixed Rossby–gravity waves triggered by lateral forcing. *J. Atmos. Sci.,* **52,** 1473–1486.

Mahlman, J. D., and L. J. Umshied, 1984: Dynamics of the middle atmosphere: Successes and problems of the GFDL "SKYHI" general circulation model. *Dynamics of the Middle Atmosphere,* J. R. Holton and T. Matsuno, Eds., Terra Scientific, 501–525.

Maruyama, T., 1994: Upward transport of westerly momentum due to disturbances of the equatorial lower stratosphere in the period range of about 2 days—A Singapore data analysis for 1983–1993. *J. Meteor. Soc. Japan,* **72,** 423–432.

Mote, P. W., and Coauthors, 1996: An atmospheric tape recorder: The imprint of tropical tropopause temperatures on stratospheric water vapor. *J. Geophys. Res.,* **101,** 3989–4006.

Nakazawa, T., 1988: Tropical super clusters within intraseasonal variations over the western Pacific. *J. Meteor. Soc. Japan,* **66,** 823–839.

Naujokat, B., 1986: An update of the observed quasi-biennial oscillation of the stratospheric winds over the tropics. *J. Atmos. Sci.,* **43,** 1873–1877.

Nishi, N., and A. Sumi, 1995: Eastward-moving disturbance near the tropopause along the equator during the TOGA COARE IOP. *J. Meteor. Soc. Japan,* **73,** 321–337.

Ogino, S., M. D. Yamanaka, and S. Fukao, 1995: Meridional variation of lower stratospheric gravity wave activity: A quick look at Hakuho-Maru J-COARE cruise rawinsonde data. *J. Meteor. Soc. Japan,* **73,** 407–413.

Peixoto, J. P., and A. H. Oort, 1992: *Physics of Climate.* American Institute of Physics, 520 pp.

Pfister, L., S. Scott, M. Loewenstein, S. Bowen, and M. Legg, 1993a: Mesoscale disturbances in the tropical stratosphere excited by convection: Observations and effects on the stratospheric momentum budget. *J. Atmos. Sci.,* **50,** 1058–1075.

——, K. R. Chan, T. P. Bui, S. Bowen, M. Legg, B. Gary, K. Kelly, M. Proffitt, and W. Starr, 1993b: Gravity waves generated by a tropical cyclone during the STEP tropical field program: A case study. *J. Geophys. Res.,* **98,** 8611–8638.

Plumb, R. A., 1977: The interaction of two internal waves with the mean flow: Implications for the theory of the quasi-biennial oscillation. *J. Atmos. Sci.,* **34,** 1847–1858.

——, and A. D. McEwan, 1978: The instability of a forced standing wave in a viscous stratified fluid: A laboratory analogue of the quasi-biennial oscillation. *J. Atmos. Sci.,* **35,** 1827–1839.

——, and R. C. Bell, 1982: A model of the quasi-biennial oscillation on an equatorial beta plane. *Quart. J. Roy. Meteor. Soc.,* **108,** 335–352.

Salby, M. L., and R. R. Garcia, 1987: Transient response to localized episodic heating in the tropics. Part I: Excitation and short-time near field behavior. *J. Atmos. Sci.,* **44,** 458–498.

Saravanan, R., 1990: A multiwave model of the quasi-biennial oscillation. *J. Atmos. Sci.,* **47,** 2465–2474.

Sato, K., and T. J. Dunkerton, 1997: Estimates of momentum flux associated with equatorial Kelvin and gravity waves. *J. Geophys. Res.,* **102** (D22), 26 247–26 261.

——, F. Hasegawa, and I. Hirota, 1994: Short-period disturbances in the equatorial lower stratosphere. *J. Meteor. Soc. Japan,* **72,** 859–872.

Takahashi, M., 1996: Simulation of the stratospheric quasi-biennial oscillation using a general circulation model. *Geophys. Res. Lett.,* **23,** 661–664.

——, and B. A. Boville, 1992: A three-dimensional simulation of the equatorial quasi-biennial oscillation. *J. Atmos. Sci.,* **49,** 1020–1035.

——, and T. Kumakura, 1995: Equatorial wave behavior in a three-dimensional sector model: Relation to the simulated QBO-like oscillation and comparison with a T21 general circulation model. *J. Meteor. Soc. Japan,* **73,** 1011–1027.

——, and M. Shiobara, 1995: A note on a QBO-like oscillation in a 1/5 sector three-dimensional model derived from a GCM. *J. Meteor. Soc. Japan,* **73,** 131–137.

——, N. Zhao, and T. Kumakura, 1997: Equatorial waves in a general circulation model simulating a quasi-biennial oscillation. *J. Meteor. Soc. Japan,* **75,** 529–540.

Takayabu, Y. N., 1994a: Large-scale cloud disturbances associated with equatorial waves. Part I: Spectral features of the cloud disturbances. *J. Meteor. Soc. Japan,* **72,** 433–449.

——, 1994b: Large-scale cloud disturbances associated with equatorial waves. Part II: Westward-propagating inertio-gravity waves. *J. Meteor. Soc. Japan,* **72,** 451–465.

Tsuda, T., Y. Murayama, H. Wiryosumarto, S. W. B. Harijono, and S. Kato, 1994a: Radiosonde observations of equatorial atmosphere dynamics over Indonesia. Part 1: Equatorial waves and diurnal tides. *J. Geophys. Res.,* **99,** 10 491–10 505.

——, ——, ——, ——, and S. Kato, 1994b: Radiosonde observations of equatorial atmosphere dynamics over Indonesia. Part II: Characteristics of gravity waves. *J. Geophys. Res.,* **99,** 10 507–10 516.

Wallace, J. M., and V. E. Kousky, 1968: Observational evidence of Kelvin waves in the tropical stratosphere. *J. Atmos. Sci.,* **25,** 900–907.

Yanai, M., and T. Maruyama, 1966: Stratospheric wave disturbances propagating over the equatorial Pacific. *J. Meteor. Soc. Japan,* **44,** 291–294.